

UNIVERSITY OF BIRMINGHAM

Corrosion and Metallographic Characterisation of Aluminium Armour Alloy AA7017-T651

Stephen Shapcott

A thesis submitted to The University of Birmingham for degree of

Master of Research (MRes)

Metallurgy & Materials

The University of Birmingham

September 2013

UNIVERSITY OF
BIRMINGHAM

University of Birmingham Research Archive

e-theses repository

This unpublished thesis/dissertation is copyright of the author and/or third parties. The intellectual property rights of the author or third parties in respect of this work are as defined by The Copyright Designs and Patents Act 1988 or as modified by any successor legislation.

Any use made of information contained in this thesis/dissertation must be in accordance with that legislation and must be properly acknowledged. Further distribution or reproduction in any format is prohibited without the permission of the copyright holder.

ABSTRACT

High strength 7xxx series Al-Zn-Mg-Cu alloys are widely used in the aerospace Industry due to their high strength to weight ratios. The high yield strength of alloys such as AA7075 or AA7074 is achieved through precipitation hardening, the highest of which can be in excess of 600MPa and are achieved through the addition of Cu. There is however a medium strength group of alloys in the 7xxx series which are characterised by their low copper levels maintained below 0.3wt% in order to prevent liquation cracking and hence allow them to be welded.

These medium strength Al-Zn-Mg(-Cu) alloys are mostly found in light weight armoured vehicles due to their weldability, low density and good ballistic performance. There is however very little published on the corrosion characteristics of these alloys and the little that exists is confined to studies of stress corrosion cracking (SCC) and weld fatigue. This work will attempt to understand the general corrosion characteristics of this alloy under free corrosion conditions and to establish in the literature the microstructure, particularly with regard the nature of the coarse intermetallics.

ACKNOWLEDGEMENTS

I would like to thank all those that helped me at the Sowerby research centre in Filton, it was a pleasure working and learning with you. Particular thanks go to Dr Steven Harris whose energy and passion were a great inspiration. Other notable people that helped me significantly with their experience and advice were Dr Pete Morgan, Dr Chris Figgures, Dr Stephen Morgan and Dr Erian Siggs.

I would also like to thank BAE Systems and the EPSRC for funding my work and providing facilities with which none of my work would have been possible. To The University of Birmingham thank you for training me for a career that I love.

Additional help and advice came from The University of Birmingham Centre for Electron Microscopy and many fruitful conversations with Prof. Geoff Scamans of Innoval Technology.

Most of all my thanks go to Dr Alison Davenport who always gave me support when I asked for it even when I didn't make it easy. Without Alison I would not have managed to get through my undergraduate degree let alone go on to write this thesis such as it is. My career now in materials and corrosion engineering is due to her hard work, patience and the opportunities she gave me.

CONTENTS

ABSTRACT i
ACKNOWLEDGEMENTS ii
CONTENTS iii
LIST OF FIGURES v
LIST OF TABLES x
1 INTRODUCTION 1
2 LITERATURE REVIEW 3
2.1 Introduction to Aluminium-Magnesium-Zinc Alloys 3
2.1.1 Strengthening Precipitates 4
2.1.2 Grain boundary precipitates 8
2.1.3 Dispersoids 8
2.1.4 Constituent particles 10
2.1.5 Composition and Microstructure of AA7017-T651 11
2.2 Corrosion of Aluminium Alloys 13
2.2.1 Corrosion of Aluminium 13
2.2.2 Corrosion Mechanisms of High Strength Aluminium Alloys 16
2.2.3 Corrosion of Al-Zn-Mg(-Cu) alloys 27
2.2.4 Effect on Corrosion Characteristics of Al-Zn-Mg(-Cu) Alloys by altering Cu Content 34
2.2.1 Stress Corrosion Cracking (SCC) and Weld Attack in 7017 36
3 EXPERIMENTAL PROCEDURE 40
3.1 Material 40
3.2 Sample Preparation 41
3.3 Characterization Techniques 41
3.3.1 Metallographic Etching 41
3.3.2 Optical microscopy 41
3.3.3 Scanning Electron Microscopy 41
3.3.4 Energy-Dispersive X-Ray Spectroscopy (EDX) 42

3.3.5 Wavelength dispersive X-Ray Spectroscopy (WDX) 42
3.3.6 Micro Hardness Testing 42
3.4 Solution Preparation 42
3.5 Electrochemical Testing 42
3.5.1 Polarization Experiments 42
3.5.2 Open Circuit Potential (OCP) Measurements 43
3.6 Reproducibility and statistical significance 44
4 MICROSTRUCTURAL AND CORROSION CHARACTERISATION OF AA7017-T651 45
4.1 Introduction 45
4.2 Microstructural characterisation 45
4.2.1 Grain structure 45
4.2.2 Through thickness variation 46
4.2.3 Coarse Intermetallic Particle Identification 49
4.3 Corrosion Characterisation 55
4.3.1 Sort Term Exposure to High Cl^- Concentration Solution 55
4.3.2 Longer Exposure to Lower Cl^- Concentration solution 57
4.3.3 Electrochemistry 62
4.3.4 Discussion 66
5 SUMMARY AND CONCLUSIONS 71
5.1 Summary and Conclusions 71
6 APPENDIX 73
6.1 Experiments in developing AA7017-T651 using Keller's reagent 73
7 REFERENCES 74

LIST OF FIGURES

Figure 1. Phase diagram of a Al-Mg-Zn ternary alloy (84).....5

Figure 2. TEM micrographs showing Al_6Mn dispersoids in a 0.3 wt% Mn Al-Zn-Mg alloy. η-$MgZn_2$ particles acted as a heterogeneous nucleation site for their formation. (18).....9

Figure 3. Aluminium corner of a binary Al-Zr phase diagram (17).....9

Figure 4. Images of AA7017-T651. a) optical images of the three orthoganal faces, the rolling direction is shown. b) TEM image of the grain boundary region. (22).....13

Figure 5. Potential-pH equilibrium diagram for aluminium and water at 25˚C. Details of the labelled lines can be found in the "*Atlas of Electrochemical Equilibria in Aqueous Solutions"* (26).....14

Figure 6. Variety in pit cross-sectional shape. (27).....18

Figure 7. Schematic diagrams representing pit initiation by three mechanisms, Penetration, Adsorption and Film Breaking. (32) adapted from (31).....20

Figure 8. Schematic cyclic polarisation curve. Pitting potential (E_P) and the repassivation potential (E_R) and labelled. (44).....21

Figure 9. Variations of pitting potential as a function of alloying element content of (a) Al-Zn, (b) Al-Mg, and (c) Al-Cu binary alloys (60, 61).....28

Figure 10. Schematic representation of initial stages of pit initiation around iron rich intermetallics during 2-3 h of immersion into aerated NaCl solution (68).....31

Figure 11. Schematic representing Cu enrichment and redistribution during localized corrosion in AA2024-T3 (71).....33

Figure 12. Effect of overaging and Cu content on SCC resistance of an Al-Zn-Mg alloy in 3.5% NaCl solution. (66).....38

Figure 13 Microstructure of three orthogonal sections of AA7017 - T651, the diagram (bottom right) depicts how each image (a), (b) or (c) corresponds to regarding the rolling direction. The surfaces have been etched in Keller's reagent for 30s. 46

Figure 14. Mean average of three Vicker's micro hardness measurements taklen through the thickness of AA7017-T651 plate. 47

Figure 15. Composition of alloying elements in AA7017-T651 as measured by EDX at 1 mm intervals across the thickness of the plate. 48

Figure 16. WDX measurements of the matrix composition of Mn, Cr and Zr at different depths within a sample of AA7017-T65151 plate. Error bars indicate the range of 5 repeat measurements taken at each depth. 49

Figure 17. SEM backscatter images depicting representative distributions of coarse intermetallic particles in AA7017-T651 in three orthogonal directions at two magnifications.....50

Figure 18. SEM backscatter image of the long transverse section of AA7017-T651 showing general distribution of coarse intermetallic particles.....50

Figure 19. Scatter plot showing composition of Al verses the composition of all other elements present in $Al_6(Fe, Mn)$ containing particles. The composition was determined using point analysis EDX. The green point shows the background composition of these elements. 51

Figure 20. Scatter plot showing composition of Si verses Mg present in Mg_2Si containing particles. The composition was determined using point analysis EDX. The green point shows the background composition of these elements. 51

Figure 21. Scatter plot showing composition of Al verses Zr + Ti present in $Al_3(Zr, Ti)$ containing particles. The composition was determined using point analysis EDX. The green point shows the background composition of these elements. 52

Figure 22. Backscattered Scanning Electron Microscope (SEM) image of AA7017- T651 in longitudinal section. $Al_6(Fe, Mn)$ particles can be seen in white.....52

Figure 23. Backscattered Scanning Electron Microscope (SEM) image of AA7017 – T651 in longitudinal section. The dark particles are Mg_2Si. 53

Figure 24. Backscattered Scanning Electron Microscope (SEM) image of AA7017- T651 in longitudinal section. $Al_3(Zr, Ti)$ particles can be seen in white.....54

Figure 25. Before and after SEM backscattered electron images of the three particle types found in AA7017-T651 in longitudinal section. Showing before and after immersion in 5wt% NaCl solution for 90 min at room temperature.....56

Figure 26. Microscope images of polished longitudinal face of AA7017-T651 after immersion in 0.1 M NaCl solution for 16 hours at room temperature. Various magnifications are shown and labelled.....58

Figure 27. Stitched microscope images of three orthogonal faces of AA7017-T651 after exposure to 0.1 M NaCl solution for 40 hours. Longitudinal face (L), long transverse (LT) face and short transverse (ST) sections are labelled. Red line indicates where samples were sectioned. 58

Figure 28. SEM backscattered electron images of long transverse section of AA7017-T651 after 40 hours immersion in 0.1 M NaCl solution at room temperature. Three magnifications are given and are labelled, 100x, 250x and 500x. White arrows indicate unknown surface deposits. 59

Figure 29. SEM micrograph taken at 30° from the normal, depicting the surface of a AA7017-T651 sample in longitudinal section after exposure to a 0.1 M NaCl solution at room temperature for 40 hours, nitric acid cleaned. 60

Figure 30. Images of increasing magnification depicting a AA7017-T651 surface in longitudinal section after exposure to a 0.1 M NaCl solution for 40 hours. a) Optical micrograph showing a Al_3(Zr, Ti) coarse intermetallic at the centre. b) and c) SEM micrographs taken at increasing magnifications of the same intermetallic. 61

Figure 31. Cross section SEM micrograph taken at 30° from the normal to the longitudinal (L) section of sample shown in Figure 29, depicting the surface of a AA7017-T651 sample after exposure to a 0.1 M NaCl solution at room temperature for 40 hours, short transverse plane labelled (ST). 61

Figure 32. Anodic polarisation curves for AA7017-T651, AA7039-T6 and AA7017-T651 in deaerated 0.5 M NaCl, pH 3.56 with a scan rate of 0.2 mV/s. (Dashed lines are taken from data from Meng (19).) 62

Figure 33. SEM image of AA7017-T651 in the short transverse section surface after polarisation beyond the E_1 breakdown potential. 63

Figure 34. Open circuit potential measurements of initial exposure of AA7017-T651 to deaerated 0.5 M NaCl solution adjusted to pH 3.56, compared with data from Meng et al. under the same conditions. (19) 64

Figure 35. Long term open circuit potential measurements of a AA7017-T651 sample exposed to 0.5 M NaCl solution pH adjusted to 3.56, at room temperature and open to the air, plotted against Meng et al. data. (19) 65

Figure 36. Secondary electron image of the surface of a sample of AA7017-T651 in the short transverse section exposed to 0.5 M NaCl solution pH adjusted to 3.56 for 336 hours. 66

LIST OF TABLES

Table 1. Some typical 7xxx series alloy compositions in wt%. AA7075 and AA7475 are classed as copper containing Al-Zn-Mg-Cu alloys, and AA7017 and AA7020 are classed as low copper Al-Zn-Mg alloys. The balance of all compositions is Al. (1) 4

Table 2. Example of some typical constituent particles found in aluminium alloys, classed by their solubility (9). 10

Table 3. Common particles found in 7xxx series alloys. 11

Table 4. Elemental composition of AA7017 aluminium alloy in wt%. The balance of the composition is Al. (1) 12

Table 5. Effect of alloying elements in aluminium alloys on overpotential and repassivation potential. (51) 30

Table 6. Breakdown potentials for AA7xxx-T6 in deaerated 0.5 M NaCl, pH=3.56 (19). 35

Table 7. ICP-AES measurements of AA7017-T651 test material in wt%. The balance is Al. 40

1 INTRODUCTION

High strength heat treatable 7xxx series Aluminium-Magnesium-Zinc (Al-Mg-Zn-(Cu)) alloys are widely used for their high strength to weight ratio. They are mainly adopted in the aerospace industry for this very property (e.g. AA7075 and AA7475), where strengths can exceed 600MPa and densities as low as 2.70 g/cm^3, less than 35% that of the density of steel.

Aluminium alloys however can suffer from localised corrosion which can cause catastrophic premature failures in service. In the case of the high strength 7xxx series alloys it has been demonstrated through much published literature that the localised corrosion behaviour of these alloys is strongly associated with the copper content, where copper levels as high as 2 wt% are added for strength and stress corrosion cracking (SCC) resistance.

There are however many low copper (up to 0.3 wt%), medium strength weldable 7xxx grades (e.g. AA7017 and AA7039), that have seen use in armoured military vehicles due to their good ballistic performance, strength to weight ratio and weldability.

These vehicles are seeing greater challenges as they face longer service lives than planned, great threats from improvise explosive devices (IEDs) and are deployed to varying and more highly corrosive environments around the world. These light weight armoured vehicles are of particular importance for getting military personnel rapidly into new arenas but keeping them safely behind primary armour protection. Corrosion is also one of the biggest through life costs to military and armed forces worldwide.

These low copper grades used in armoured vehicles have remained little studied in comparison to those containing higher copper, and the low copper levels leave questions around the initiation and propagation mechanisms of corrosion.

It is the aim of this thesis to better characterise the corrosion character of AA7017-T651 alloy (Cu 0.2 wt% max). This work will also attempt to link the corrosion characteristics with the microstructure and chemistry of the alloy through multiple characterisation techniques. An attempt will also be made to place AA7017-T651 within the context of other 7xxx series grades and their corrosion properties.

2 LITERATURE REVIEW

2.1 Introduction to Aluminium-Magnesium-Zinc Alloys

Pure aluminium has very low yield strength (7-11 MPa), which is the stress at which the material begins to deform plastically. Its strength can be increased by alloying with metals such as Cu, Mg, Mn and Zn.

High strength 7xxx series Aluminium-Magnesium-Zinc (Al-Mg-Zn-(Cu)) alloys are widely used for their high strength to weight ratio. They can be split into two groups the high strength high Cu non-weldable alloys (e.g. AA7075 and AA7475) and the weldable medium strength low Cu alloys (e.g. AA7017 and AA7039). Cu also has the ability to reduce the susceptibility to stress corrosion cracking (SCC) which is common in the low Cu weldable alloys, however it does increase the general corrosion susceptibility. Much work has been done to characterise the corrosion characteristics of the high Cu 7xxx series alloys, however the second group containing little copper (<0.2 wt%) has little published on the general corrosion characteristics. The high Cu alloys are typically used in aerospace applications where mechanical fixing is employed, whereas the low Cu alloys are found in military land vehicle applications where their weldability and good ballistic performance are exploited.

Table 1 contains the typical chemistries of some common 7xxx series alloys. This work focuses on the peak aged T6 condition, which is solution heat treated and artificially aged. The AA7017-T651 grade used in this work had also undergone stretching of up to 3% to help relieve internal stresses; this is signified by the Tx51 designation.

Table 1. Some typical 7xxx series alloy compositions in wt%. AA7075 and AA7475 are classed as copper containing Al-Zn-Mg-Cu alloys, and AA7017 and AA7020 are classed as low copper Al-Zn-Mg alloys. The balance of all compositions is Al. (1)

Alloy	Zn	Mg	Cu	Mn	Cr	Ti	Zr	Fe	Si
AA7075	5.1-6.1	2.1-2.9	1.2-2.0	0.30	0.18-0.28	0.20	-	0.50	0.40
AA7475	5.2-6.2	1.9-2.6	1.2-1.9	0.06	0.18-0.25	0.06	-	0.12	0.10
AA7017	4.0-5.2	2.0-3.0	0.20	0.05-0.50	0.35	0.15	0.10-0.25	0.45	0.35
AA7020	4.0-5.0	1.0-1.4	0.20	0.05-0.50	0.10-0.35	-	0.08-0.20	0.40	0.35
AA7039	3.5-4.5	2.3-3.3	0.10	0.10-0.40	0.15-0.25	0.10	-	0.40	0.30
AA7004	3.8-4.6	1.0-2.0	0.05	0.20-0.70	0.05	0.05	0.10-0.20	0.35	0.25

2.1.1 Strengthening Precipitates

Both the Al-Zn-Mg and the Al-Zn-Mg-Cu alloys are heat treatable and strengthening is achieved through precipitation hardening. Under artificial aging from supersaturated solid solution spherical GP zones less than 1 nm in size form in 7xxx series alloys. The peak age (highest strength) is reached in the T6 temper where semi-coherent intermediate phase precipitates are produced (2). At higher temperatures and longer aging, overaging occurs in the T7 temper where the incoherent equilibrium phase is produced, and hence there is a slight drop in strength from the T6 to the T7 temper.

Figure 1 shows the aluminium corner of the Al-Mg-Zn phase diagram, lines marked with temperatures indicate the temperature at which different concentrations of Mg and Zn are in solid solution in the aluminium.

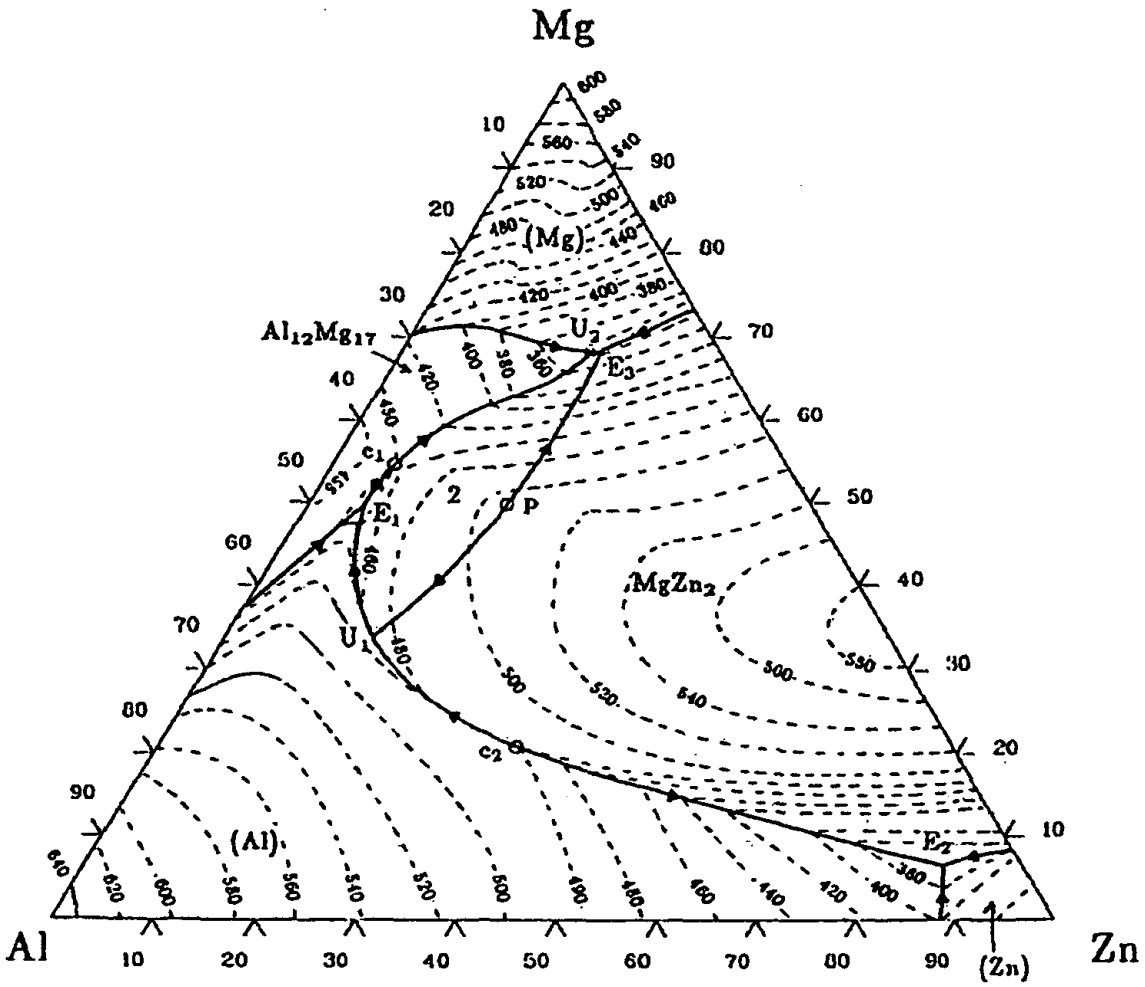


Figure 1. Phase diagram of a Al-Mg-Zn ternary alloy (84).

It is not expected that a difference exists between the nature of precipitates formed in between a material in the T6 or the T651 temper. This is because there is no real difference in the aging behaviour between the stretched T651 and the un-stretched T6 (3-5).

The dominant alloying elements involved in precipitation hardening of 7xxx series alloys are Zn and Mg. In ternary Al-Zn-Mg alloys the type of precipitate formed is dependent on the ratio of Zn to Mg. Two different homogeneous phases can be produced under equilibrium conditions. A Zn/Mg ratio greater than 2 produces η (eta) phase $MgZn_2$ (6), i.e. stoichiometry. The η phase forms in coarse plates in the hexagonal close packed structure in

7xxx series alloys (7-10). If naturally aged only GP zones are formed in the final material (10). In the T6 and T651 condition the η' (eta prime) phase is the strengthening phase (2, 10, 11).

$$\boldsymbol{\alpha_{ssss} \rightarrow \text{GP zones (spherical)} \rightarrow \eta' \rightarrow \eta}$$

A Zn/Mg ratio less than 2 gives a stable precipitate of $Mg_{32}(Al, Zn)_{49}$, this is called T (tau) phase and it has a cubic structure in 7xxx series alloys (7, 8).

$$\boldsymbol{\alpha_{ssss} \rightarrow \text{GP zones (spherical)} \rightarrow T' \rightarrow T}$$

The quaternary Al-Zn-Mg-Cu 7xxx series alloys have copper added to give additional strength, where yield strengths for up to 600 MPa can be achieved (10). The addition of copper has an effect on the chemistry of the strengthening precipitates. Copper is soluble in both the η and T phases producing $Zn(Al, Cu, Zn)_2$ and $Mg_{32}(Al, Cu, Zn)_{49}$ respectively. Starke proposed that $ZnMg_2$ and AlMgCu are in an isomorphous series, with increasing volume fractions of AlMgCu phase as the copper content is increased (8). Aluminium and copper being so soluble in the η phase that they substitute for zinc (6).

It is well known that increasing copper content increases the volume fraction of strengthening precipitates and causes them to form in a finer dispersion; this has the effect of further strengthening copper rich alloys in the peak aged condition (10-12). Sarkar et al. states that in the T651 condition copper affects the nature of the precipitates, stating that the degree of coherency of strengthening precipitates in Al-6Zn-2Mg alloys can be affected by copper content (11). They state that in the T651 condition, low copper alloy precipitates are coherent with the matrix. It would follow therefore that precipitates are sheared by transient dislocations upon deformation. In copper rich Al-6Zn-2Mg alloys, the strengthening

precipitates are partially coherent and incoherent (11), implying a mixture of looping and shearing of dislocations. Sarkar et al. also states that in the T7 condition the strengthening precipitates in both the copper rich and low copper alloy are incoherent. Hence, dislocations will tend to loop around the strengthening phase. This fits with what we know of the equilibrium phases often being incoherent with respect the matrix (13).

Work by Chinh et al. states that in Al-Zn-Mg alloys mainly spherical GP zones are formed. In Al-Zn-Mg-Cu alloys additional ellipsoidal GP zones are also formed; only the ellipsoidal GP zones being rich in Cu. They state that the ellipsoidal GP zones are more readily used as nucleation sites for the η' phase.

Work on 7050 alloys by Sha and Cerezo agrees that Cu content in the ellipsoidal GP zones is slightly higher than the spherical ones and state that it may be involved in the initial clustering process. They also state that the ellipsoidal GP zones are slightly Zn rich (Zn/Mg ratio ≈1.1) and that the η' phase that forms on them is also Zn rich (Zn/Mg ratio ≈1.2) (14).

It is known that the shape of a GP zone is likely related to the crystallographic plane on which it forms (9). It can be implied from this that the additional strengthening precipitates are being caused to form on an additional crystallographic plane by the addition of Cu.

In summary, Cu additions to 7xxx series alloys increase the volume fraction of strengthening precipitates; this contributes to the hardening of the alloys. It is also known that precipitates with a higher aspect ratio have a greater strengthening effect. Therefore both Chinh et al. and Sha et al. indicate that the additional strengthening given to Cu containing Al-Zn-Mg alloys is partially due to the shape of the precipitates formed due to Cu.

2.1.2 Grain boundary precipitates

Heterogeneous precipitation at the grain boundary also occurs in 7xxx series alloys, (see Figure 2). These precipitates are typically ~50-100 nm in the T6/T651 condition (10, 15). Their formation creates precipitate free zones (PFZ) adjacent to the grain boundaries, where solute atoms and vacancies are depleted in the PFZ. The width of the PFZ is closely related to the quench rate after heat treatment, the slower the cooling rate, the wider the PFZ. It follows logically that this is due to the rate of diffusion of the solute atoms towards the grain boundary, a slower cooling rate giving more time and energy for diffusion.

2.1.3 Dispersoids

Submicron dispersoid particles (0.05-0.5 μm) precipitate during the homogenisation heat treatment (9). They are formed from elements which are slow diffusers in solid aluminium, such as Cr, Mn and Zr, and once formed are relatively insoluble (9, 10). They suppress recrystallisation by the Zener drag effect. Zener drag is where incoherent particles resist the motion of grain boundaries past them. This is caused by the large interface energy associated with an incoherent particle (13). If grain boundary movement is restricted then this will serve to limit grain growth.

Typical examples of dispersoids in 7xxx series alloys are Al_3Zr, Al_6Mn, $Al_{12}Mg_2Cr$ and $Al_{20}Cu_2Mn_3$ (9, 10). Zirconium is the most efficient of the dispersoid forming elements, and is commonly added to retard recrystallisation (9, 10, 16). Al_3Zr will readily dissolve Ti (Figure 3) and it is common to find $Al_3(Zr,Ti)$ in alloys which contain both Zr and Ti (17).

Figure 2 shows Al_6Mn dispersoids formed in a 0.3 wt% Mn Al-Zn-Mg alloy, on slow heating to the homogenisation temperature. The dispersoids formed heterogeneously on η-$MgZn_2$ particles. Grain boundary precipitates and a PFZ can also be seen (9).

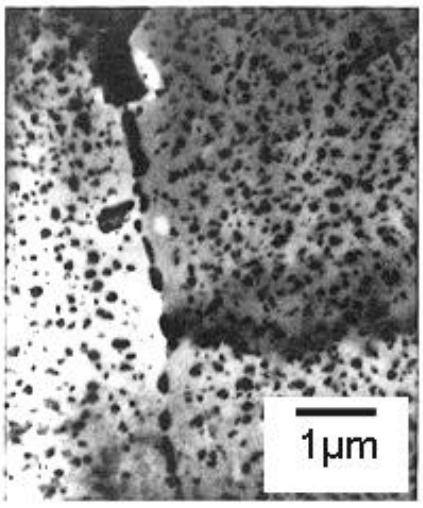


Figure 2. TEM micrographs showing Al_6Mn dispersoids in a 0.3 wt% Mn Al-Zn-Mg alloy. η-$MgZn_2$ particles acted as a heterogeneous nucleation site for their formation. (18)

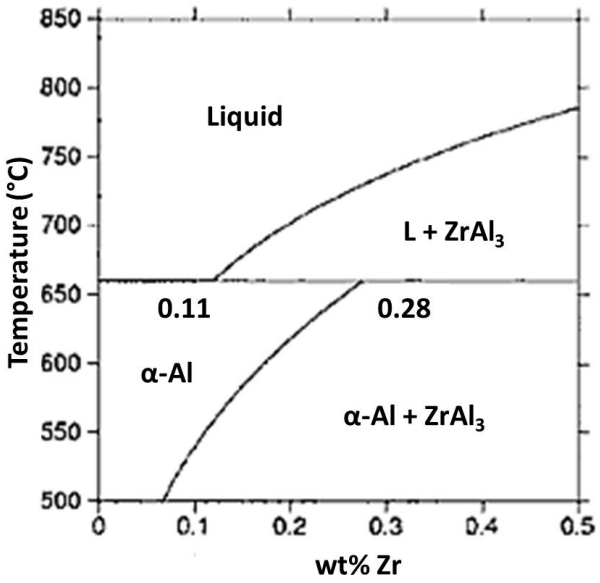


Figure 3. Aluminium corner of a binary Al-Zr phase diagram (17).

2.1.4 Constituent particles

Constituent particles are coarse intermetallics which form interdendritically upon casting (9). They are impurities in the alloy microstructure and although undesirable they are tolerated. They form through eutectic decomposition, and come in two categories, soluble constituents and insoluble constituents. The insoluble constituents usually contain iron and/or silicon, and the soluble constants are usually compounds of the major alloying elements (9). The soluble constituents are usually removed through homogenisation heat treatment. The insoluble constituents remain after homogenisation, but are broken into 0.5-10 micron pieces through rolling. These pieces form in clusters called 'stringers', aligned with the rolling direction (9).

Table 2. Example of some typical constituent particles found in aluminium alloys, classed by their solubility (9).

Typical soluble constituents	Typical insoluble constituents
Al_2Cu, S-Al_2CuMg, Mg_2Si	Al_3Fe, $Al_6(Fe,Mn)$, Al_7Cu_2Fe, α-Al(Fe,Mn,Si)

Constituent particles have a number of detrimental effects. Firstly, their brittle nature allows them to fracture within a strained ductile aluminium matrix. This fracture and their incoherency with the matrix allows for a stress concentration field to form within the material at the crack tip (9). This causes a decrease in toughness of the material. Secondly, these intermetallics have a detrimental effect on the corrosion properties, as is explained in section 2.3.

Table 3. Common particles found in 7xxx series alloys.

Classification	Size	Composition
Hardening precipitates	< 0.1 µm	η-$Mg(Al, Zn, (Cu))_2$ (6, 7, 9, 19) T-$Mg_{32}(Al, Zn, (Cu))_{49}$ (7, 10)
Dispersoids	0.05 – 0.5 µm	Al_3Zr (9, 10, 20, 21), $Al_{12}Mg_2Cr$, Al_6Mn (9), $Al_{20}Cu_2Mn_3$ (9, 10)
Constituent particles/ inclusions	0.5 – 10+ µm	Al_3Fe, $Al_3(Fe,Si)$, $Al_3(Fe,Cu,Si)$, Al_2CuMg, $Al_3(Fe,Cu)$, Mg_2Si, Al_7Cu_2Fe (19), Al_6Fe, Al_3Mn, $Al_3(Fe,Mn)$, $Al_6(Fe,Mn)$, $Al_6(Mn,Cu)$, $Al_{23}CuFe_4$, Al_7Cu_2Fe, α-AlFeSi, α-Al(Fe,Mn)Si, α-AlMnSi (9), $Al_3(Zr,Ti)$ (17), $Al_{20}Cu_2Mn_3$ (10)

2.1.5 Composition and Microstructure of AA7017-T651

AA7017-T651 is a medium strength Al-Zn-Mg alloy mainly employed in structural applications such as lightweight bridges and armoured vehicles, where its weldablility is a key property. Little is published directly relating to AA7017; what does exist is focused on the structural characteristics of the material, either under stress corrosion cracking conditions or corrosion after welding (both explained in section 2.2.1). Almost nothing is mentioned in the literature regarding the as received microstructure or common precipitates in AA7017 in any temper condition. There is also little or nothing in the literature relating to general corrosion characteristics of the alloy. The Aluminium Association designated composition of AA7017 is shown in Table 4.

Table 4. Elemental composition of AA7017 aluminium alloy in wt%. The balance of the composition is Al. (1)

Si	Fe	Cu	Mn	Mg	Cr	Ni	Zn	Ti	Zr
0.35	0.45	0.20	0.05-0.50	2.0-3.0	0.35	0.10	4.0-5.2	0.15	0.10-0.25

One piece of work by Mukhopadhyay gives us some clues as the microstructure of AA7017-T651 (22), all other information must be gathered from alloys of similar composition and temper. Figure 4 shows optical micrographs of all three orthogonal faces, as well as a Transmission Electron Microscope (TEM) image of a grain boundary of AA7017 in the T651 condition, taken from Mukhopadhyay (22). The optical micrographs show a highly fibrous partially recrystallised microstructure, where the grains are flattened perpendicular to the rolling direction. Grains appear to be in the order of 100s of microns wide and only 10s of microns deep. The TEM image shows fine strengthening precipitates in the grain body, with a maximum size of 10s of nm. Mukhopadhyay states that these are η′ precipitates. The TEM image also shows grain boundary particles, we are told that these are η particles. It is evident that the grain boundary η particles are incoherent to the observed grains next to them due to their lens shapes (13). A precipitate free zone can also be seen adjacent to the grain boundary in the TEM image.

Literature relating to many other Al-Zn-Mg alloys was reviewed to give incite as the likely microstructure and precipitates present in 7017. These alloys included 7003, 7004 (19), 7005, 7010, 7018, 7020, 7039 (19), 7079, 7108, 7179 and unclassified low Cu (<0.2 wt%) Al-Zn-Mg alloys. The most similar alloys compositionally to 7017 are 7018, 7020 and 7039.

Meng et al. studied a number of 7xxx series alloys with a range of Cu contents (15, 19). They identified the only coarse intermetallic in AA7039 to be Al_3(Fe, Si). The alloys

studied with Cu contents above this had Cu containing intermetallics such as S-phase. This indicates that 7017 will also contain the insoluble $Al_3(Fe, Si)$ coarse intermetallic.

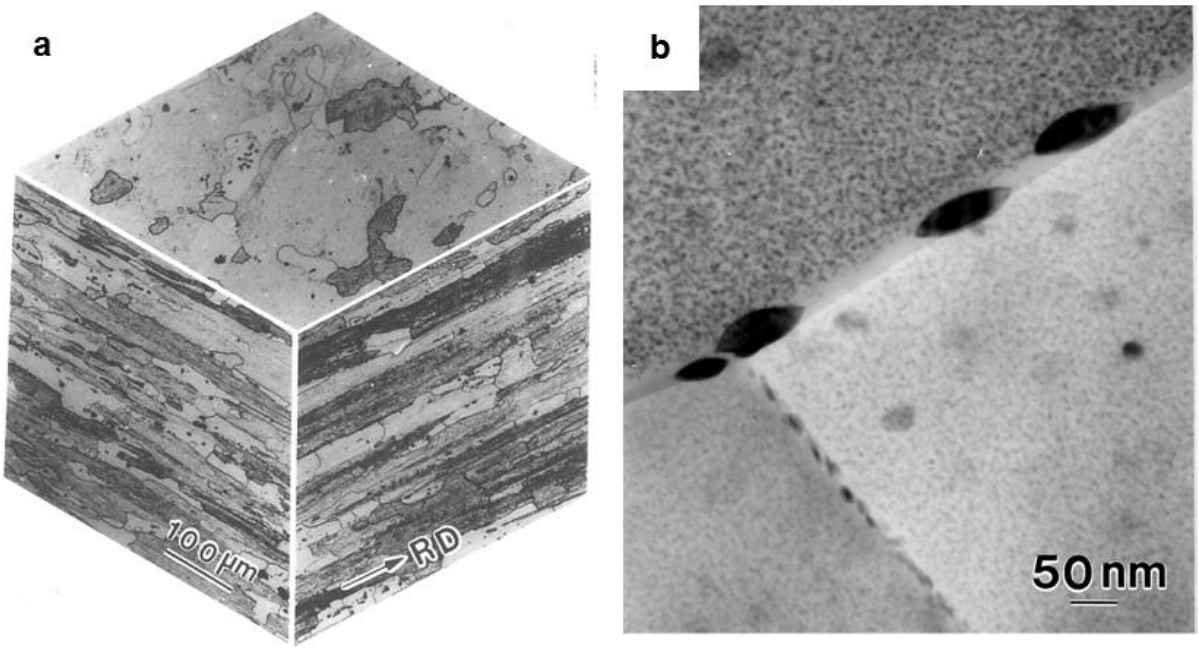


Figure 4. Images of AA7017-T651. a) optical images of the three orthoganal faces, the rolling direction is shown. b) TEM image of the grain boundary region. (22)

2.2 Corrosion of Aluminium Alloys

2.2.1 Corrosion of Aluminium

Corrosion can be defined as the deterioration of a material's properties due to its interaction with its environment (23). Pure aluminium is excellent at resisting this deterioration in most environments as it is protected by a persistent oxide film which forms on its surface in the oxidation reaction:

$$2Al + 3H_2O \rightarrow Al_2O_3 + 6H^+ + 6e^- \qquad \textbf{Equation 1}$$

The layer that forms is typically 1-10nm thick (24), porous on the outer surface and dense near the interface with the aluminium (25). In general this oxide layer protects against

corrosion by acting as a physical barrier from the environment and an electrical insulator, preventing electrochemical reactions. The oxide film will reform within seconds in most oxygen containing environments if damaged, dependent on pH and temperature (9).

This passive oxide layer is however only stable between pH 4.5 and 8.5 (26), as aluminium alloys are amphoteric and can dissolve in both strong acid or alkali solutions. The stability of the passive oxide layer at varying potentials is shown in the aluminium-water Pourbaix diagram (Figure 5).

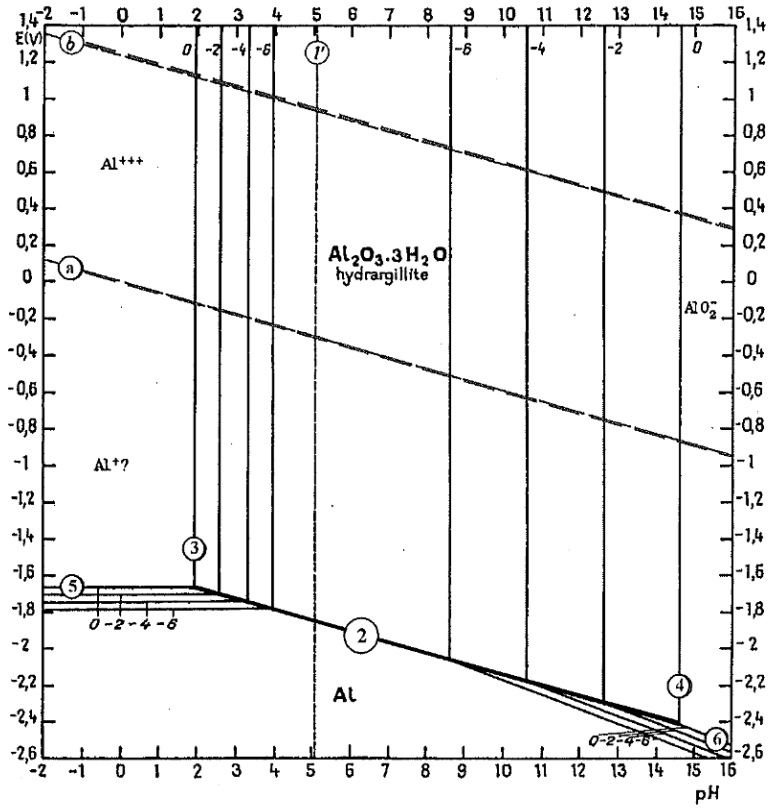


Figure 5. Potential-pH equilibrium diagram for aluminium and water at 25˚C. Details of the labelled lines can be found in the *"Atlas of Electrochemical Equilibria in Aqueous Solutions"* (26).

When the passive oxide layer is exposed to acidic solutions it dissolves by the following equation:

$$Al_2O_3 + 6H^+ \rightarrow 2Al^{3+} + 3H_2O$$ **Equation 2**

Once the oxide layer is removed in acid conditions the aluminium substrate dissolves by:

$$Al \rightarrow Al^{3+} + 3e^-$$ **Equation 3**

In alkaline solutions aluminium dissolves by:

$$Al_2O_3 + 3H_2O + 2OH^- \rightarrow 2Al(OH)_4^-$$ **Equation 4**

Once the oxide layer is removed in alkali conditions the aluminium substrate dissolves by:

$$Al + 4\ OH^- \rightarrow Al(OH)_4^- + 3e^-$$ **Equation 5**

In most service conditions aluminium alloys are not exposed to these extremes of pH, but neither are they protected by a continuous and flawless oxide film. This is because when aluminium is alloyed above solid solution precipitates form within the material. Where these precipitates break the surface of the alloy a thinner less protective oxide film grows on them and they allow for transport of electrons to the solution allowing electrochemical reactions to take place (24).

Corrosion is usually the removal of material through anodic dissolution. In aluminium this is the dissolving of aluminium ions into solution:

$$Al \rightarrow Al^{3+} + 3e^-$$ **Equation 6**

To balance the charge the electrons produced in this reaction must be consumed in a cathodic reduction reaction. These typically take the form of the reduction of either water:

$$2H_2O + 2e^- \rightarrow 2OH^- + H_2$$ **Equation 7**

or the reduction of oxygen:

$$O_2 + 2H_2O + 4e^- \rightarrow 4OH^-$$ **Equation 8**

The changes in solution chemistry local to the anodic and cathodic sites can also contribute to the corrosion process. Hydrolysis of Al^{3+} from anodic dissolution (Equation 6) causes the acidification of the local solution through production of H^+ ions:

$$Al^{3+} + H_2O \rightarrow AlOH^{2+} + H^+$$ **Equation 9**

Hydroxide ions produced in the cathodic reactions (Equations 7 & 8) causes a increase in pH local to the cathodic sites resulting in alkaline dissolution:

$$Al + 4OH^- \rightarrow Al(OH)_4^- + 3e^-$$ **Equation 10**

2.2.2 Corrosion Mechanisms of High Strength Aluminium Alloys

As described in the previous section, alloying of aluminium has a detrimental effect it's the corrosion characteristics. Some of the most highly alloyed and consequently highly prone to corrosion are the high strength aluminium alloys, which include the 2xxx and 7xxx series alloys. The alloying of aluminium can result in the formation of intermetallic precipitate particles within the material as described in section 2.1.1. This heterogeneity in the material allows for corrosion in discrete areas of the alloys surface, this is called localised corrosion. One such mechanism of localised corrosion is pitting corrosion.

2.2.2.1 Pitting Corrosion in Pure Aluminium

Pitting is localised accelerated dissolution of a metal in the form of pits. It is an autocatalytic phenomenon whereby the internal solution within the pit gradually gets more aggressive due to a drop in pH (Equation 9) and an increase in aggressive ion (e.g. halides) concentration, typically chloride (Cl^-). The role of chloride means that pitting is more likely in chloride containing environments. Negative chloride ions are drawn in due to charge balancing with the outside solution as more and more positive Al^{2+} ions are generated in the pit. This low pH and high Cl^- concentration results in sustained corrosion as the internal surfaces of the pit are prevented from repassivating. Pits can form many shapes as shown in Figure 6. Microstructure can also play a key role in the morphology of the pits that form (Figure 6f). Often they have a small opening at the surface with a relatively large volume subsurface (Figure 6d). This can make pits particularly dangerous when a material's integrity is safety critical as a large amount of attack can go overlooked.

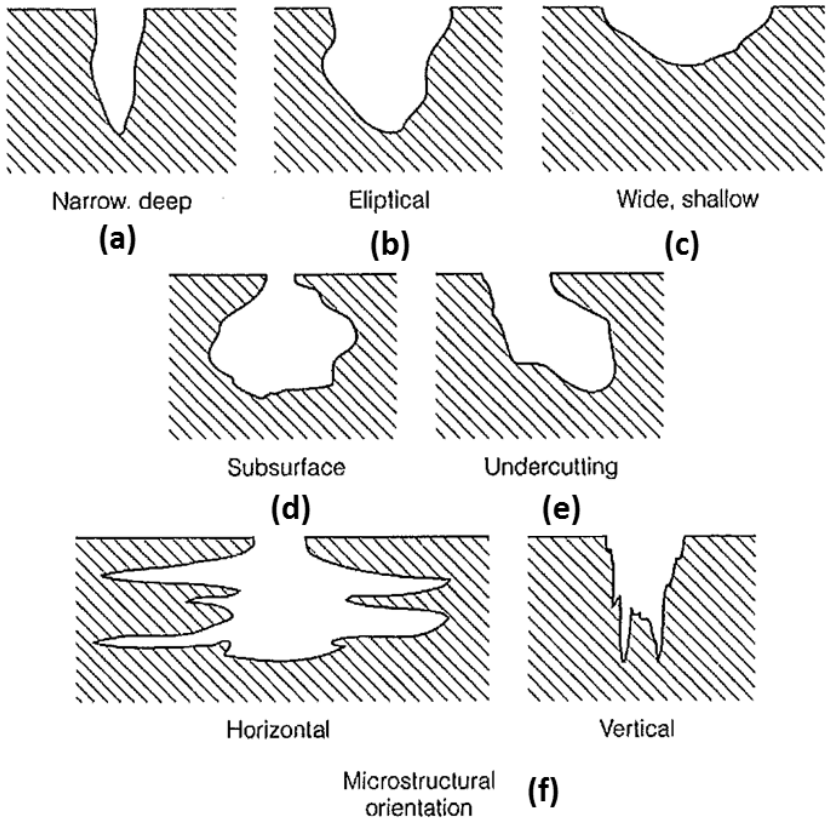


Figure 6. Variety in pit cross-sectional shape. (27)

2.2.2.2 Pit Initiation

The initial breakdown of the oxide layer is known to generally occur at or near to sites of local heterogeneity. These include second phase particles, inclusions, solute segregated grain boundaries, flaws, mechanical damage or dislocations (28). The most common of these to act as pit initiation sites in high strength aluminium alloys are intermetallic/constituent particles (29). First however, we must consider passive film breakdown in pure aluminium without the existence of intermetallic particles. This is because it can be considered that the passive film covering the matrix of an aluminium alloy will be similar to that of pure aluminium. Although it should be noted that this is not always the case, as alloying additions have been known to change the nature of the oxide film (30).

Many theories of pit initiation have been proposed (28, 31-40), however most fall into three categories as summarised by Frankel (32). Schematic diagrams of these mechanisms are shown in Figure 7. They include:

1. Penetration Mechanism, which state that aggressive anions are transported through the passive oxide layer to the metal beneath where dissolution can occur.

2. Adsorption Mechanism, where local thinning of the passive film is induced by some local adsorbed species which leads to local increases in electric field strength. Leading to passive film breakdown and pit formation.

3. Film Breakdown Mechanism, assumes the passive film is in a constant state of breakdown and repair. The stresses caused in the surface oxide from electrostriction and surface tension allowing local breakdown to occur. In passive environments these flaws would quickly heal, but in aggressive environments could propagate into a stable pit.

None of these pitting models alone can fully describe all the pitting phenomena found in metal alloys.

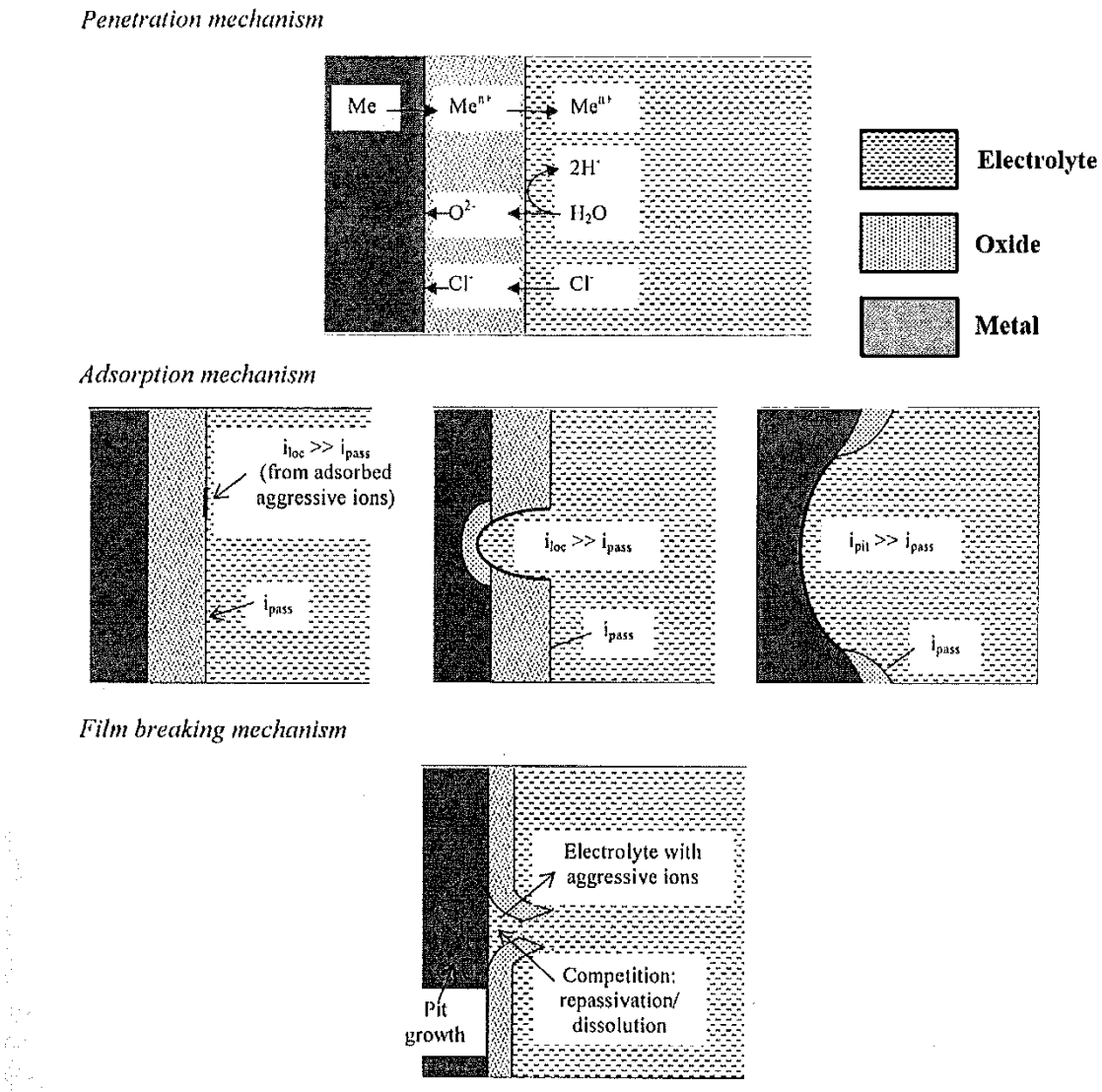


Figure 7. Schematic diagrams representing pit initiation by three mechanisms, Penetration, Adsorption and Film Breaking. (32) adapted from (31)

2.2.2.3 Metastable pitting

It is known that not all pits initiated will survive to become autocatalytic. Pits that form and then repassivate are called metastable pits (32, 36). Passivation or stabilisation are dependent on local potential and solution chemistry in and around the pit (33). Metastable pits in aluminium are in the order of sub microns to a few microns, existing for only seconds or less. They can exist below the pitting potential (associated with stable pit formation) and are found to be more frequent close to the pitting potential, as seen in the schematic of a

polarisation curve in Figure 8(36). Although much work has focused on metastable pitting in stainless steels since its discovery in the early 1970's (41), little work has been done on metastable pitting in aluminium alloys. Although Pride and co-workers (42) working on pure aluminium found that frequency of metastable pitting events increased the closer to the pitting potential they measured and with increasing chloride concentration. Detailed studies suggest that the initial growth of stable pits is identical to that in metastable pits (32), thus allowing for initial passive oxide breakdown studies to be conducted below the pitting potential. Frankel (32) suggests that metastable pit repassivation is due to rupture in the porous passive film remnant covering the pit, thus allowing the aggressive solution environment to be flushed out. This theory is supported by the rapid nature of the repassivation seen in metastable pit current transients (43). Metastable pits are not considered a corrosion risk in themselves but a firm understanding of them may give a good insight into stable pit formation and initiation.

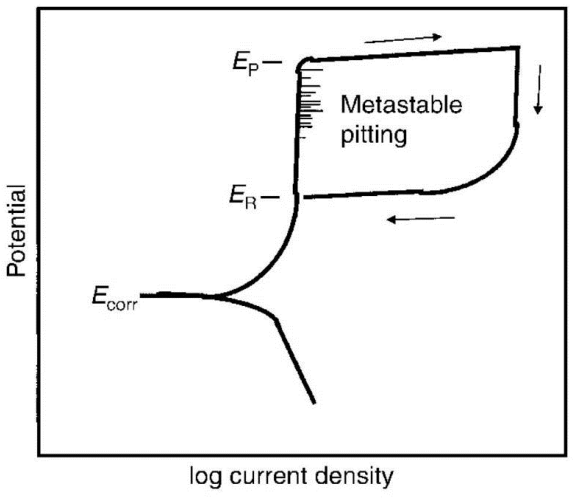


Figure 8. Schematic cyclic polarisation curve. Pitting potential (E_P) and the repassivation potential (E_R) and labelled. (44)

2.2.2.4 Pit Growth

Pit growth rate is dependent on the composition of the alloy, the solution chemistry in and around the pit, as well as the potential at the pit bottom. Three factors influence pit growth, charge transfer, ohmic control, and mass transport (45-48). These factors are dependent on five variables, potential (E), current (I), current density (i), time (t) and pit radius/depth (r). Charge transfer being related to Tefel's law, ohmic control to Faraday's law and mass transport being related to Fick's law (32).

The relationship between these variables can be hard to distinguish when many are unknown. For instance pits do not often grow in a hemispherical shape and pit radius (r) will be continually changing, thus making pit current density (i) difficult to assess. Therefore some researchers have made artificial pits by embedding a wire in epoxy, which works well for iron (49). This technique does however encounter problems with aluminium testing due to the evolution of hydrogen gas at the corrosion front. Therefore many (50, 51) have used artificial crevice electrodes which allow the escape of H_2 bubbles. These studies have indicated that pits in both materials grow in two ways. Either under mass transport control with a salt film covering the corrosion front or under ohmic control in an active state with no salt film.

2.2.2.5 Pit stability

Pit stability is governed by the chemistry within the pit; if the pit can be kept at a low enough acidity then the pit will be stable. This acidity is linked with the rate of hydrolysis (Equation 9) within the pit. Galvele found there to be a critical acidification to sustain pit growth in 1D pits, which was the product of pit depth and current density being greater than

10^{-2} A/cm (33). Pride and co-workers found that pits in pure aluminium would only be stable if they had a ratio of I_{pit}/r_{pit} greater than 10^{-2} A/cm (42). Williams and co-workers found that for stainless steel the I_{pit}/r_{pit} ratio must be greater than 4×10^{-2} A/cm (52).

Trueman argues that the work of Galvele and Pride is too simplistic in real life applications, as they use cylindrical shape pits with only an active pit bottom and do not account for pit caps (53). Trueman used a statistical method to determine the probability a metastable pit will form into a stable one in AA2024-T3. It was deduced that the size a metastable pit must achieve before becoming stable in AA2024-T3 was 13.7 µm in diameter for a hemispherical pit. This agrees with the findings of Pride et al. for pure aluminium (42).

The presence of chloride in the environment also helps to stabilise pits as it too helps to destabilise the passive oxide layer of the aluminium. I mechanism for this is suggested by Frankel, where $AlCl_3$ or aluminium oxy-chlorides such as $Al(OH)_2Cl$ and $Al(OH)Cl_2$ form a salt film. This salt film acts as a buffer or ionic species, which dissolve into the pit maintaining aggressive conditions within the pit, such as low pH (32).

2.2.2.6 Intergranular Corrosion

As well as pitting corrosion, high strength aluminium alloys are also generally very susceptible to intergranular corrosion (IGC). IGC is the selective attack of the grain boundaries or the region closely adjacent to the grain boundaries, with minimal or no attack to the grain interior. This phenomenon is attributed a difference in electrode potential between the grain boundary region and the interior of the grain. IGC is well known to be common in high strength aluminium alloys such as AA2014-T3 and AA7075-T6. The difference in electrode potential is correlated to the precipitation of microstructural

heterogeneities at grain boundaries. These heterogeneities at the grain boundaries take the form of grain boundary precipitates and a precipitate free zone (PFZ); these can be seen in Figure 4. Differences in the electrochemical behaviour of the precipitates, PFZ and the alloy matrix are suspected to drive the IGC process.

Three models have been proposed to explain the IGC process:

1. *The Galvanic Couple Model*

This states that the difference in corrosion potential (E_{corr}) between the grain boundary region and the grain interiors sets up a galvanic couple. Differences in corrosion potentials of the grain boundaries and the grain interiors of AlCu alloys have been found (54-56). Cocks and Brummer found that widening the PFZ through aging caused an increase in corrosion rate but not IGC susceptibility, suggesting that not only the galvanic model is responsible (54). Galvele and DeMicheli found that IGC does not occur in all ion conducting solutions, however if the galvanic couple model is true then this would not be the case (56).

2. *The Precipitate Free Zone (PFZ) Breakdown Model*

This is based on the work by Galvele and DeMicheli (56), they proposed that IGC is due to differences in breakdown potential (E_{pit}) between the matrix and the PFZs. This work was however only conducted in AlCu alloys and it is not clear that this is the only mechanism at play.

3. *The Anodic Dissolution of Grain Boundary Precipitates*

This model states that the grain boundary precipitates act as net anodes and dissolve preferentially to the rest of the grain. This has been observed in an AlMg alloy where the Mg_5Al_8 grain boundary precipitates dissolved resulting in IGC and IGSCC (57). Anodic dissolution of grain boundary precipitates has also been seen in AlLiCu alloys where the T1 ($CuAl_2Li$) phase underwent anodic dissolution (58).

It is likely that aspects of all three of these models play a role in IGC as no one model has been found to satisfy all experimental observations.

2.2.2.7 Exfoliation Corrosion

Exfoliation corrosion is a particular form of IGC where layers for the metal surface are delaminated from the bulk. This is due to a corrosion front progressing parallel to the surface creating voluminous corrosion product that lifts off the surface layers. Exfoliation corrosion is anisotropic in direction due to anisotropy in the grain structure of the material, caused by flattening of the grains through rolling during processing.

2.2.2.8 Stress Corrosion Cracking (SCC)

Stress corrosion cracking is the brittle fracture of usually ductile materials while under non-critical loading in a critical corrosive environment. It is neither the stress on the material or the corrosion alone which causes the brittle failure but the combination of the two. SCC can be intergranular or transgranular in nature, where the intergranular SCC follows the path of sensitised grain boundaries. In aluminium alloys SCC is almost always intergranular in nature. In fact IGC susceptibility is a prerequisite to SCC susceptibility.

There are three things required for SCC to take place, 1. Some form of tensile stress (e.g. loading or internal stresses), 2. A critical environment, different materials become susceptible to SCC due to specific chemical species in the environment (most commonly chloride induced), 3. A susceptible alloy, not all alloys or tempers are susceptible to SCC, although it is common in high strength aluminium alloys.

The SCC process can be split into three distinct stages, initiation, propagation and failure. The initiation of SCC is not well understood, but it is generally accepted that stress corrosion cracks will initiate at surface defects such as pits or intergranular corrosion. The final brittle failure of a stress corrosion crack is in many ways identical to a traditional brittle failure, and will not be discussed further. The majority of work on SCC mechanisms has been focused on the propagation mechanisms.

There have been many propagation mechanisms proposed for SCC, which is found in both the 5xxx and 7xxx series alloys. No one mechanistic explanation is satisfactory for all conditions; making it likely that the precise mechanism is very complex and dependant on precise conditions. It is found that one mechanism fits better than another in an individual environment, or occasionally a mixture of mechanisms. Three commonly accepted models have been proposed, Anodic dissolution, Hydrogen embrittlement and Mg depleted zones. None will be discussed further, as it is thought that Anodic dissolution only applies to 5xxx series alloys which have β phase (Al_3Mg_2) present at the grain boundaries (59), and Hydrogen embrittlement and Mg depleted zone models are also not directly relevant as the later stages of corrosion are not explored in this work.

2.2.3 Corrosion of Al-Zn-Mg(-Cu) alloys

2.2.3.1 Effect of Alloying Elements

In order to understand the effect of each alloying element on the corrosion behaviour of aluminium alloys Muller and Galvele analysed a number of binary alloys of Aluminium. The electrochemical potentials of various compositions of Al-Zn, Al-Mg, and Al-Cu binary alloys in deaerated 1 M NaCl were measured (60, 61) (Figure 9).

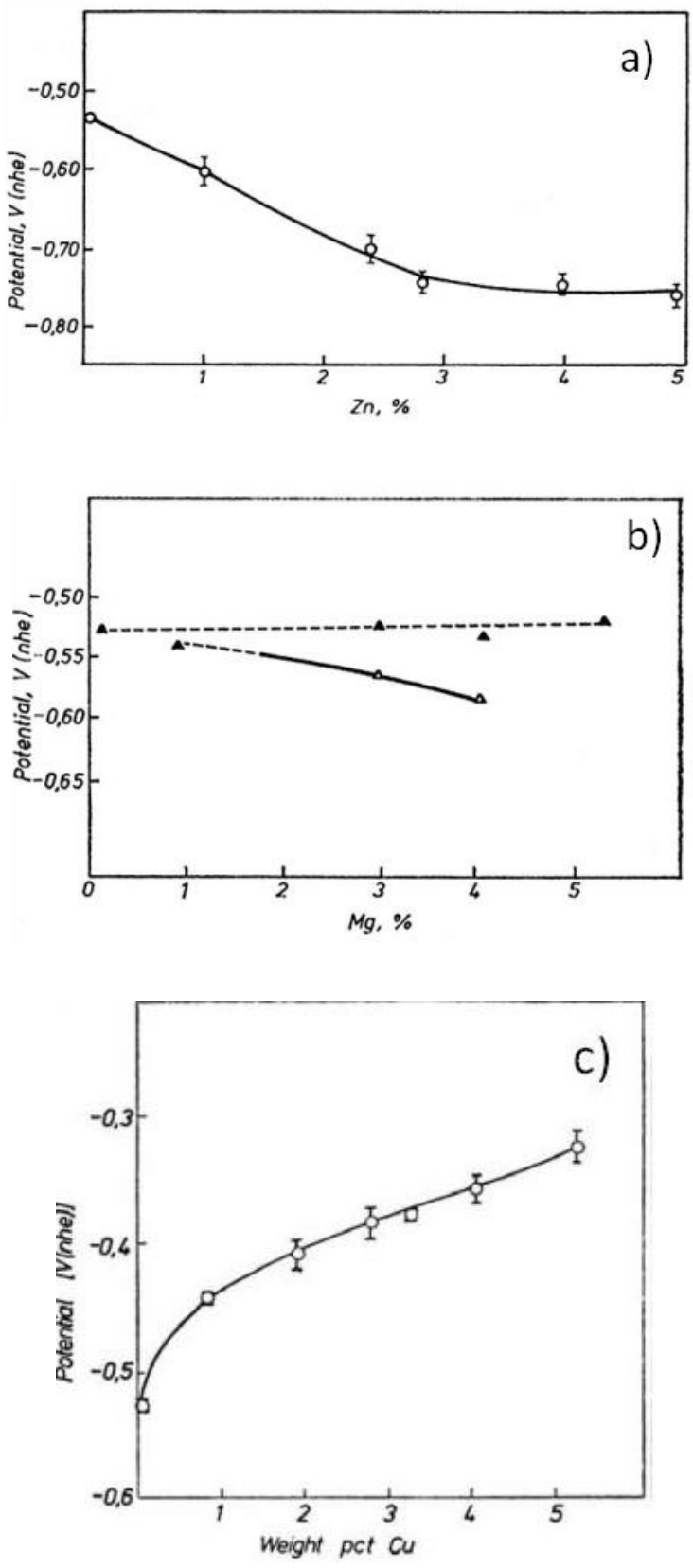


Figure 9. Variations of pitting potential as a function of alloying element content of (a) Al-Zn, (b) Al-Mg, and (c) Al-Cu binary alloys (60, 61).

Increasing Zn content up to 3wt% decreased the pitting potential, but did not decrease beyond this up to 5wt%. The Mg content up to 5wt% showed little influence on pitting potential. The addition of Cu up to 5wt% showed an initial rapidly increasing in pitting potential up to 1wt% and a steady linear increase after that. Microscope examination of the 3wt% binaries of these alloys showed tunnel like pits in the Al-Zn alloy, and crystallographically shaped pits on Al-Mg and Al-Cu. Sato and Newman suggest that pit growth rather than pit nucleation is influenced by Zn content through the study of metastable pitting on Al-Zn alloys. As they found that pit nucleation was independent of Zn content.

It has been found through electrochemical experimentation that aluminium matrix pitting potential can be greatly improved by the addition of alloying elements that are kept in SSSS (62-65). It is thought that enrichment of the passive film may slow the movement of chloride ions through to the bulk matrix. It should be noted however that Smialowska (66) proposed that the alloying additions reduced the susceptibility of the oxide film to attach fully due to the acidic conditions in the pit interior. Whichever mechanism, it is clear that alloying additions can alter the pitting probability of aluminium alloys.

An artificial crevice electrode technique was used by Ramgopal and Frankel (51) on the Al-Zn, Al-Mg and Al-Cu binary alloys. They found that the alloying additions altered the overpotential and this in turn altered the repassivation potentials as summarised in Table 5.

Table 5. Effect of alloying elements in aluminium alloys on overpotential and repassivation potential. (51)

Alloying element	Overpotential	Repassivation Potential
Zn	Decrease	Increase
Mg	No Change	No change
Cu	Decrease	Increase

2.2.3.2 Intermetallic Particles

Intermetallic particles such as the ones in Table 3 can decrease an alloys resistance to corrosion via different mechanisms dependant on their classification. Intermetallic particles can be classed into two groups, fine precipitates (which include strengthening particles, dispersoids and grain boundary precipitates) and coarse intermetallic particles (which include constituent particles and inclusions). The coarse intermetallic particles are formed or present during solidification whereas the fine precipitates develop during aging. The nature of the intermetallics varies with alloy composition and heat treatment. Section 2.2.2.6 earlier covers the role of the fine precipitates in the corrosion of aluminium alloys.

The coarse intermetallic particles can be described as either being active or noble relative to the Al matrix. The range of particle chemistries and difference in electrochemical properties from the matrix can be striking. This can be seen in the comprehensive review of coarse intermetallics compiled by Buchheit (67) which lists the corrosion potentials of each type of particle.

Figure 10 shows a step by step representation of the pit initiation mechanism via the presence of cathodically active noble intermetallic particles taken from work done by Park and co-workers (68). This work focused on alloy 6061 and the role of the Al_3Fe constituent

particles. The Al_3Fe particles were found to be noble relative to the matrix and supported oxygen reduction. This resulted in loss of material in the matrix adjacent to the particles due to a locally high pH which results on alkaline dissolution, this phenomena will in this work be referred to as cathodic grooving. This is shown to initiate pitting, but the environment of the groove must somehow switch from an alkaline chemistry to that of an acid one for a stable pit to be established.

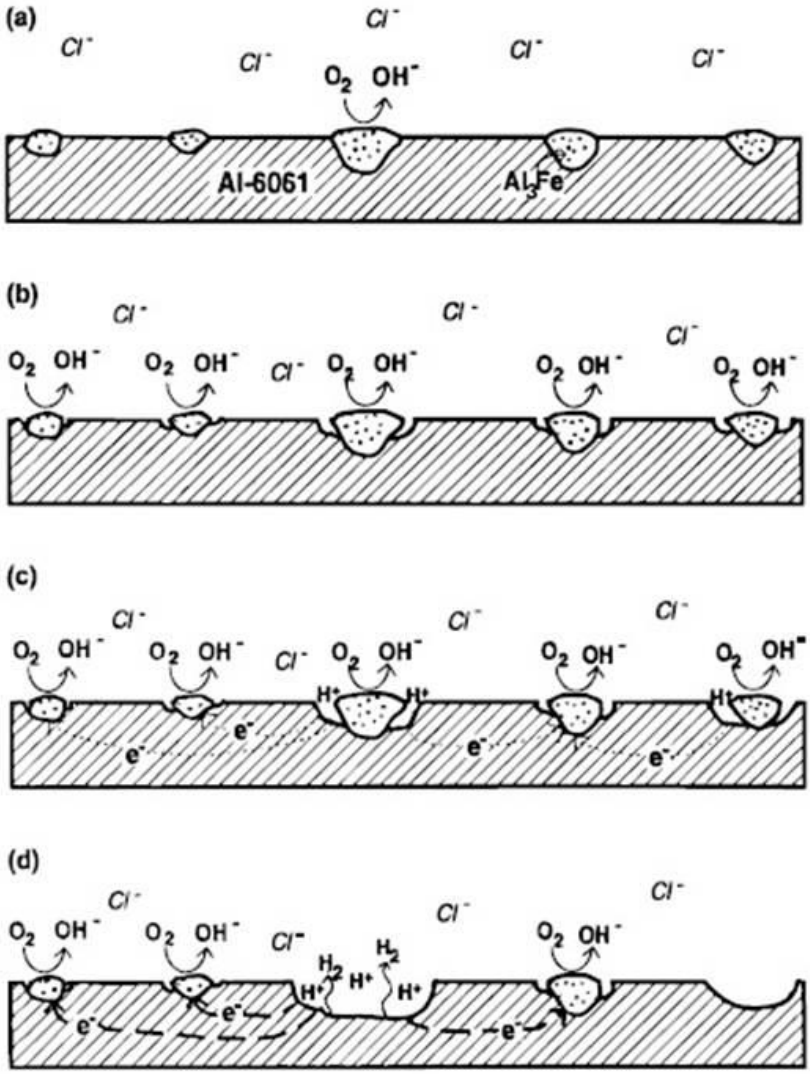


Figure 10. Schematic representation of initial stages of pit initiation around iron rich intermetallics during 2-3 h of immersion into aerated NaCl solution (68).

Both Mg-containing Mg_2Si (β) and Al_2CuMg (S) phases act as anodes relative to the matrix, and are found to be prone to active dissolution or Mg dealloying when exposed to acidic or chloride solutions (67, 69-74). It has been found that S phase (Al_2CuMg) in AA2024-T3 undergoes selective dissolution of Mg and Al when under both anodic and cathodic polarisation (69, 71-74). This dealloying left Cu-rich remnants which were noble relative to the matrix and so produced cathodic grooving followed by pitting at the site of the dealloyed S phase particle. Buchheit and others (69, 71-74) suggested that corrosion was accelerated by Cu release and redistribution from the S phase and has been supported by rotating ring-disk electrode (RRDE) experiments.

It can be seen therefore that alloy chemistry and the phases that form through heat treatment play a key role in the corrosion of aluminium alloys, and that Cu enrichment and redistribution is of some importance.

2.2.3.3 Cu Enrichment and Redistribution

As mentioned earlier Cu enrichment and redistribution from Al_2CuMg S phase particles has been suggested to enhance corrosion in the 2xxx series alloys, it therefore follows that this mechanism may also be present in the Cu containing 7xxx series alloys. The noble nature of Cu relative to the matrix of these alloys leads to cathodic regions on the surface necessary for localised corrosion to take place.

Figure 11 shows a graphical representation of the enrichment and redistribution mechanism. It has been found that in either chloride rich or acidic solutions S phase can undergo dealloying (71), where dissolution of Mg and Al from the particle leaves Cu rich sponge remnants. It has been proposed by Buchheit et al. that the dealloying process allows

for mechanical freeing of the Cu rich remnants which in turn allows for their movement away from the site of the intermetallic through convection. This can explain how the Cu rich surface regions can form below the reversible potential for Cu/Cu^{2+}, as once they are electrically isolated from the bulk alloy they can be oxidised to Cu^{2+} ions which then reduce back to atomic Cu if they come into contact with the alloy surface again. Rotating ring-disk electrode (RRDE) experiments maintain this hypothesis when conducted below the reversible potential for Cu/Cu^{2+} (69).

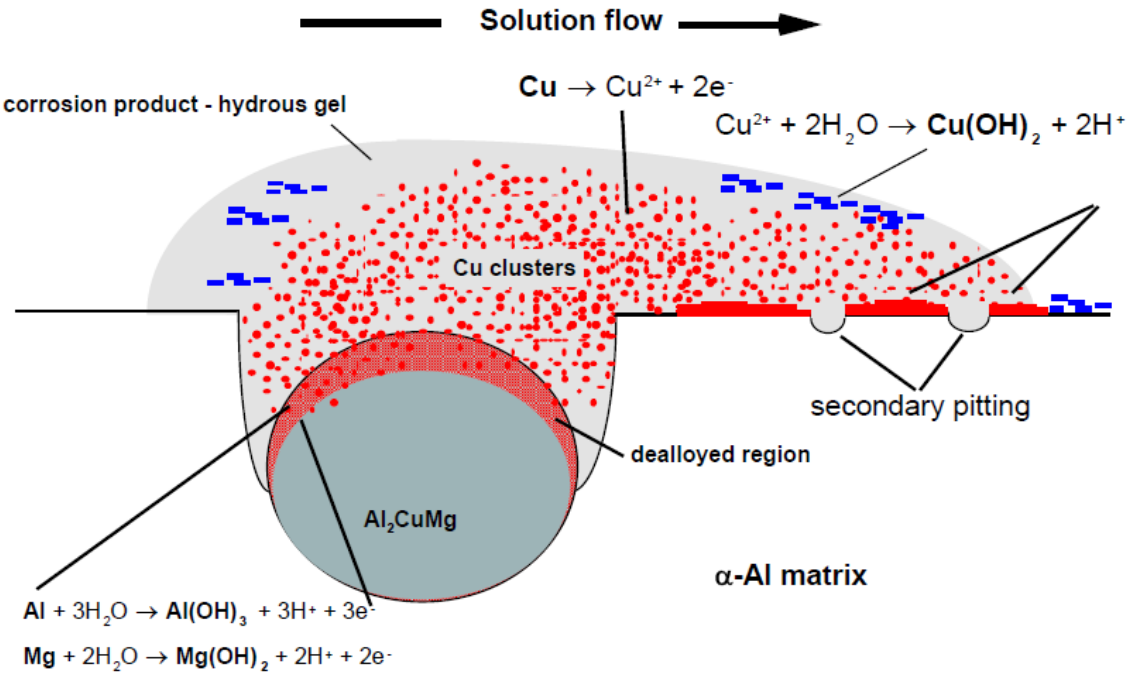


Figure 11. Schematic representing Cu enrichment and redistribution during localized corrosion in AA2024-T3 (71).

Another mechanism by which Cu ions can be released from S phase below the reversible potential for Cu/Cu^{2+} has been proposed by Dimtrov et al. (75, 76). They suggest that the Cu ions have sufficient energy to be freed from the surface of the intermetallics due to the curvature effect, thus moving the reduction potential to be more anodic. They found

that a radius of 40 nm was sufficient to shift the reduction potential into the region where Cu ion formation is possible (76).

It has also been suggested that Cu freed from the matrix rather than the intermetallics could also lead to Cu enrichment on the surface (75, 77). The cathodic Cu sponge remnant left behind after dealloying could lead to alkaline dissolution adjacent to the intermetallic. It is suggested that during this dissolution of the matrix somehow the Cu in the matrix is left behind on the surface. It is possible that both mechanisms hold true and that Cu enrichment comes from both the matrix and the intermetallics. Work done utilising a rotating ring-disk electrode (RRDE) (69) indicates that initially the redistribution of Cu from S phase dominates whereas over longer periods it is the dealloying of the matrix which dominates.

2.2.4 Effect on Corrosion Characteristics of Al-Zn-Mg(-Cu) Alloys by altering Cu Content

Almost all published research on low copper (<0.2 wt%) 7xxx series alloys (Al-Zn-Mg) focuses on either stress corrosion cracking (SCC) or on weld attack, which will be discussed below. A fully comprehensive study of the corrosion mechanism for un-stressed and un-welded material has yet to become available; this work attempts to go some way to filling that absence. As the corrosion mechanisms discussed above in section 2.2.3 for high Cu aluminium alloys all rely on the presence of Cu, it is of value to investigate the mechanism for low Cu alloys too, as the methods for preventing corrosion in these alloys may differ. It can also be assumed that the role of intermetallic particles in AA7017 will also

be important in the corrosion mechanism, however little is published on the fine precipitates and nothing on the coarse intermetallics found in this alloy.

Work by Meng (19) studied the effect of Cu content on the corrosion properties of 7xxx series alloys. Five alloys of increasing Cu content were chosen, their breakdown potentials can be seen in Table 6. All the alloys exhibited two breakdown potentials, except for 7004 which had effectively zero Cu. The initial breakdown potential E_1 is due to the transient dissolution of an active surface layer created in polishing and described in more detail by Zhijun (78). The breakdown potential at E_2 is associated with combined IGC and selective grain attack.

Table 6. Breakdown potentials for AA7xxx-T6 in deaerated 0.5 M NaCl, pH=3.56 (19).

Alloy	Cu content (wt %)	E_1 (mV SCE)	E_2 (mV SCE)	E_2-E_1 (mV)
7004	0.013	N/A	-951 ± 3	N/A
7039	0.077	-905 ± 4	-835 ± 6	70
7029	0.69	-821 ±3	-766 ± 1	55
7075	1.36	-780 ± 4	-720 ± 2	60
7050	2.00	-751 ± 3	-699 ± 1	52

Under free corrosion conditions in aerated chloride solutions Meng (19) found that corrosion potential increases with Cu content, and polarisation resistance decreases with Cu content. This is due to Cu enrichment on the surface causing greater oxygen reduction. Meng concludes that Cu content is overall detrimental to the corrosion characteristics of the alloys (19). The work also concluded that the low Cu alloys 7004 and 7039 would not undergo sustained localised attack, as after a few days both of their OCP values had dropped very low. 7039 and 7017 have a similar Cu content and they are however found to undergo

severe IGC in service conditions on land vehicles, therefore there must be conditions which will facilitate corrosion in these alloys.

2.2.1 Stress Corrosion Cracking (SCC) and Weld Attack in 7017

As mentioned earlier SCC has been well studied in 7017, this is due to it having good general corrosion resistance, so any failure is usually due first to SCC attack. As 7017 is a structural alloy there is usually some form of tensile loading on the alloy plate. Residual stresses within the plate are also introduced through the welding process; this helps to give an opportunity for SCC in the 'white zone' which is the interface between the weld bead and the HAZ (79, 80). The dominance of SCC in failure of these alloys has meant that research regarding 7017 has focused in this area (94-106); however nothing has been published on the general corrosion characteristics of this alloy or the mechanism of initiation.

Holroyd, Scamans and Kotsikos have all proposed that SCC is initiated from grain boundaries in the 'white zone' of welds. They also propose that elevated concentrations of hydrogen at the crack tip are correlated with increased SCC (79). There is evidence that thermal treatment such as that found next to a weld promotes movement of Mg towards the grain boundaries (9, 79). This Mg rich region then acts as a site for localised corrosion, which generates both hydrousoxide and nascent hydrogen. This free hydrogen then migrates into the adjacent grain boundary eventually causing embrittlement of the boundary when sufficient hydrogen has accumulated. This area of embrittled material can then undergo a burst of brittle fracture when stressed, thus exposing further material to corrosion and resultant hydrogen rich environment allowing the process to continue.

Al-Zn-Mg alloys such as 7017 are designed to be weldable, this has meant that Cu levels must be kept below 0.3% to prevent hot-cracking (liquation cracking) during weld solidification (9). Lower Cu also helps to reduce the general corrosion and pitting corrosion susceptibility. The lower Cu levels however make the alloy highly susceptible to SCC. It is also known that increasing Mg + Zn value in these alloys increases SCC susceptibility but also increases strength, therefore it is necessary to find the middle ground between these properties when selecting an alloy chemistry (9). It is thought that Mg + Zn value should not exceed 6% in order to have acceptable resistance to SCC. Gruhl found that Zn:Mg ratio was important in achieving SCC resistance, he found that a ratio between 2.7 and 2.9 was optimum (81).

7017 is also known to be susceptible to attack from the short transverse (ST) section of rolled plate. This is due to the fully non-recrystallized nature of the grain structure, where the grain structure is highly anisotropic with very elongated grains in the direction of rolling. The grain boundaries of these grains penetrate deep into the plate meaning that SCC and exfoliation corrosion are more favourable. A process has been developed to protect the end grain sections of the plate; this process is known as ‘buttering’. Buttering is a type of welding process where weld/filler material is applied to the end of the plate. This process acts as a barrier from corrosive environments and alters the grain boundary microstructure to an equiaxed one. The thermal cycle introduced by buttering also relieves the internal stresses in the end of the plate thus helping to mitigate against SCC, as the end plate is un-restrained and so is free to remove any internal stress. The type of welding rod used for buttering is Al-5% Mg (82).

Figure 12 shows the relationship between copper content and temper and their effect of SCC resistance within aluminium alloys. A copper addition of 1% helps dramatically to slow the crack velocity and similarly so does over-aging to the T7 temper (66).

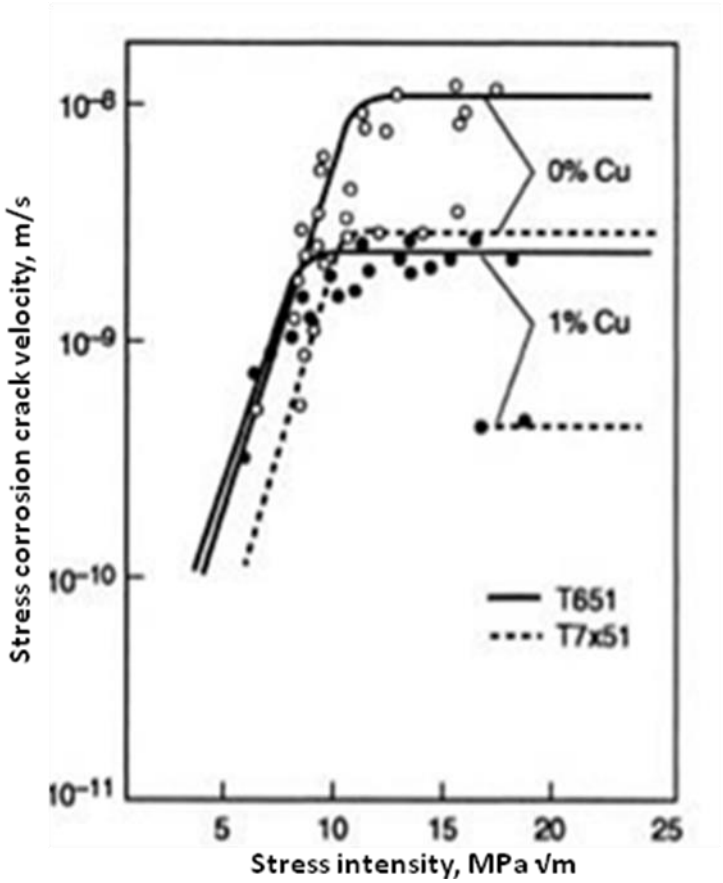


Figure 12. Effect of overaging and Cu content on SCC resistance of an Al-Zn-Mg alloy in 3.5% NaCl solution. (66)

General exfoliation corrosion has also been observed in the HAZ (79, 80). This is due to the fact that 7xxx series alloys are generally electronegative compared to the weld bead, which is the reverse to most weldable aluminium alloys. This means that the parent material is attacked preferentially to the weld. The susceptibility of the HAZ to initiation of exfoliation corrosion has led to a novel method of protecting this area from the environment. A

thermally sprayed aluminium coating is applied to the areas adjacent to the weld line to maintain 7017 welds within the 'safe potential zone' and thus reduce corrosion. Another approach is to alter the weld material chemistry to cause it to become electronegative with respect to the parent material, this has been achieved in experimentation through addition of varying proportions of indium, tin and gallium (83).

3 EXPERIMENTAL PROCEDURE

3.1 Material

AA7017-T651 material was supplied by Alcan UK and was manufactured to be compliant to MODUK DEF STAN 95-31 and all tests were conducted in the as received condition. Alloy chemistry was taken from the mill certificate which was also confirmed through inductively coupled plasma atomic emission spectroscopy (ICP-AES) by a UKAS (United Kingdom Accreditation Service) accredited third party test house (Table 7).

Table 7. ICP-AES measurements of AA7017-T651 test material in wt%. The balance is Al.

Si	Fe	Cu	Mn	Mg	Cr	Ni	Zn	Ti	Zr
0.029	0.092	0.191	0.251	2.54	0.153	0.755	4.231	0.035	0.100

The sample material was solution treated at 455°C for 1.5 h, quenched in water at ambient temperature followed by artificial aging to the peak-aged condition through 8 h at 100°C followed by 24 h at 120°C. The T651 condition involves solution heat treatment and stress relieved by stretching (permanent set 1.5 to 3% for sheet and plate), then artificially aged.

As the mil certificate indicated the material passed all required testing under DEF STAN 95-31 and would have met the requirements of the following assessments:

- Ballistic Assessment
- Mechanical Properties
- Chemical Composition

- Weldability
- Long Transverse Stress Corrosion Resistance
- Short Transverse Stress Corrosion Resistance

3.2 Sample Preparation

AA7017-T651 samples were mounted in epoxy and polished to a 1 μm diamond finish in non-aqueous media, Struers DP-Lubricant yellow.

3.3 Characterization Techniques

3.3.1 Metallographic Etching

3.3.1.1 Keller's Etch

Metallographic preparation was performed on three orthogonal orientations by sectioning then polishing to a 1 μm finish with a diamond suspension using an alcohol based lubricant. Etching was performed using Keller's reagent, 1 HF:1.5 HCl:2.5 HNO_3:95 H_2O, by volume.

3.3.2 Optical microscopy

Optical images were taken using a Carl Zeiss Axioplan microscope fitted with a selection of lenses of varying magnification. The camera and software are supplied by Struers.

3.3.3 Scanning Electron Microscopy

Secondary electron and backscatter electron images were taken using a Leo 1450-VP scanning electron microscope (SEM).

3.3.4 Energy-Dispersive X-Ray Spectroscopy (EDX)

EDX measurements were taken using a Leo 1450-VP scanning electron microscope (SEM) equipped with an Oxford Instruments Inca X-act, at a working distance of 15mm and at 20 kV. Figure 15 shows the through thickness composition of AA7017-T651 plate as measured using a 1 mm area EDX scan at 1 mm intervals.

3.3.5 Wavelength dispersive X-Ray Spectroscopy (WDX)

WDX measurements were taking at the University of Birmingham Centre for Electron Microscopy on a JEOL 7000F fitted with Wave WDS.

3.3.6 Micro Hardness Testing

Vickers micro hardness testing was conducted with a 15 second dwell time and a mass of 300g.

3.4 Solution Preparation

All solutions were made fresh on a daily basis and fresh solution was used in each experiment. Solution pH was measured regularly with a calibrated pH probe and pH adjusted with dilute $HCl_{(aq)}$. Salinity was adjusted through addition of $NaCl_{(s)}$ only. Where 0.5 M NaCl solutions with pH adjusted to 3.56 are used, this chemistry was chosen to match that of the work done by Meng and co-workers in order for results to be directly comparable. Reproducibility of Meng values was confirmed through parallel testing of AA7075-T6 (19).

3.5 Electrochemical Testing

3.5.1 Polarization Experiments

Electrochemical polarization measurements were performed on samples ground to 1200 grit just prior to testing. The tests were conducted at room temperature in flat cells

with an exposure area of 1cm^2. The electrolyte solution used was 0.5M NaCl solution pH adjusted to pH 3.56 by the addition of HCl. The solution was sparged with Ar to reduce the corrosion potential and allow clear observation of the breakdown potential. Measurements were made using an ACM Gill AC potentiostat. A Pt counter electrode and a Ag/AgCl reference electrode were used. The scan rate was 0.2 mV/s. The corrosion morphologies and surfaces were examined metallographically after exposure to determine the nature of the attack.

3.5.2 Open Circuit Potential (OCP) Measurements

OCP measurements were performed on samples ground to 1200 grit just prior to testing. The tests were conducted at room temperature in flat cells with an exposure area of 1cm^2. The electrolyte solution used was 0.5M NaCl solution pH adjusted to pH 3.56 by the addition of HCl. The solution was open to the air. Measurements were made using an ACM Gill AC potentiostat. A Pt counter electrode and a Ag/AgCl reference electrode were used. The corrosion morphologies and surfaces were examined metallographically after exposure to determine the nature of the attack.

3.6 Reproducibility and statistical significance

Reproducibility was of upmost importance during experimentation, therefore many repeat experiments were made. All values given are either averages, and will have associated error bars, or will have been repeated a minimum of three times and found to be consistent.

Plots of electrochemical data is chosen to be representative of a minimum of 5 measurements and any values taken from them are the average of all 5 or more plots with percentage error given.

Micrographs were also chosen to be representative of the surfaces and features encountered.

Errors bars were scrutinised to determine if the found variations in results could be deemed to be within accepted known variation and therefore systematic errors discovered.

4 MICROSTRUCTURAL AND CORROSION CHARACTERISATION OF AA7017-T651

4.1 Introduction

In this chapter the microstructural and chemical characteristics of the as-received AA7017-T651 material will first be identified. This is for two reasons, firstly to confirm the provenance of the material and secondly to establish the microstructural features of the alloy as there is no known published literature specific to the microstructure of AA7017-T651. The corrosion behaviour will then be studied and compared the work of Meng (15, 19) on the influence of Cu in the corrosion behaviour of 7xxx series alloys. Various electrochemical techniques such as open circuit measurement and potentiodynamic polarisation will be employed along with surface analysis and microscopy. The corrosion behaviour will then be associated to the microstructure that was identified.

4.2 Microstructural characterisation

4.2.1 Grain structure

Figure 13 depicts the orthogonal metallographic microstructure of AA7017-T651 in the T651 condition. The alloy has an elongated grain structure in the direction of rolling; this is produced through the cold rolling and stretching defined by the Tx51 temper regimen. Keller's reagent was used to develop the grain boundaries. Although the grain structure was made clear by the etching the grain boundaries were not fully developed due to the alloying element Zr which retards the recrystallization of the alloy favouring a fibrous or lamellar grain structure with poorly defined grain boundaries. (A different etch chemistry and varying etch times were tried to achieve better results these are shown in Appendix 6.1).

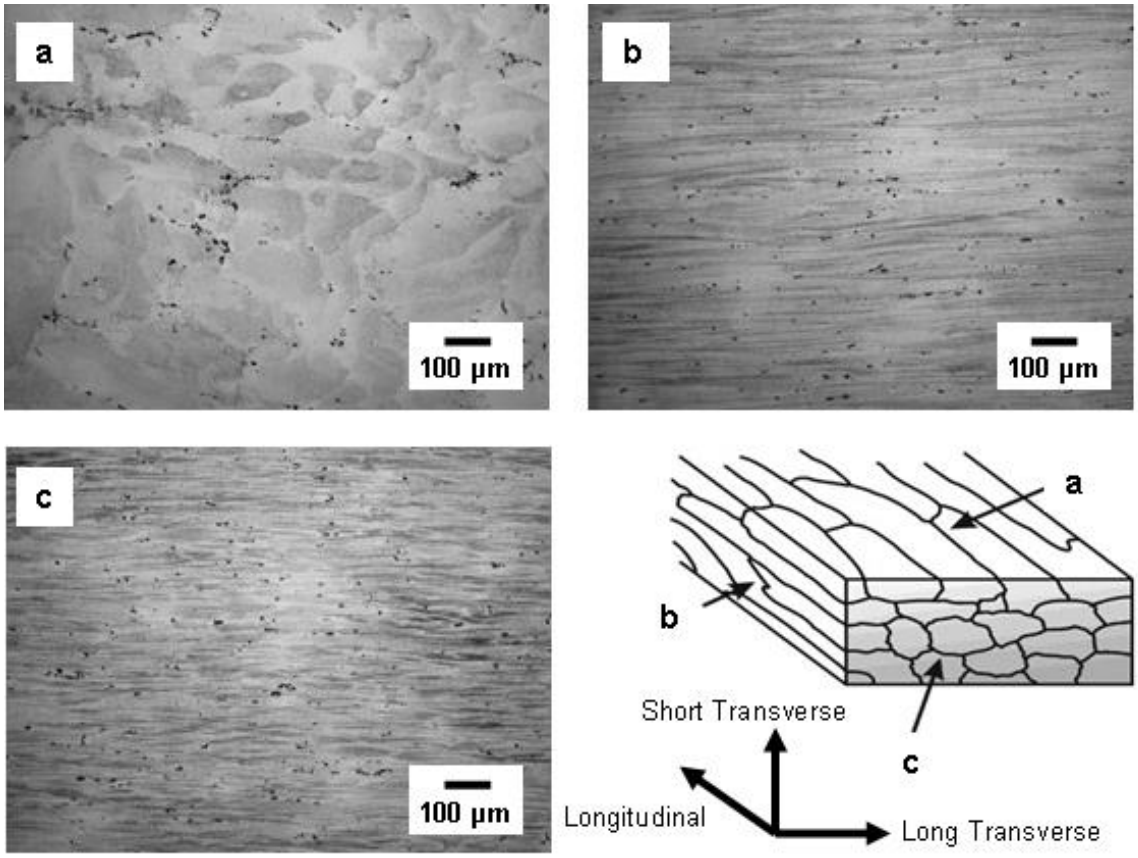


Figure 13 Microstructure of three orthogonal sections of AA7017 - T651, the diagram (bottom right) depicts how each image (a), (b) or (c) corresponds to regarding the rolling direction. The surfaces have been etched in Keller's reagent for 30s.

4.2.2 Through thickness variation

Plate homogeneity was of upmost concern to maintain consistent results under corrosion testing. The plate supplied was relatively thick (30mm); therefore through thickness variation was a possibility. Visual inspection via optical microscope and statistical analysis of constituent particle distribution was conducted; no through thickness variation was found. Through thickness hardness testing was also conducted to assess if there was a variation in strengthening precipitates, which would not be resolvable through microscope inspection. The results of these tests are shown in Figure 14, again no significant variation was found.

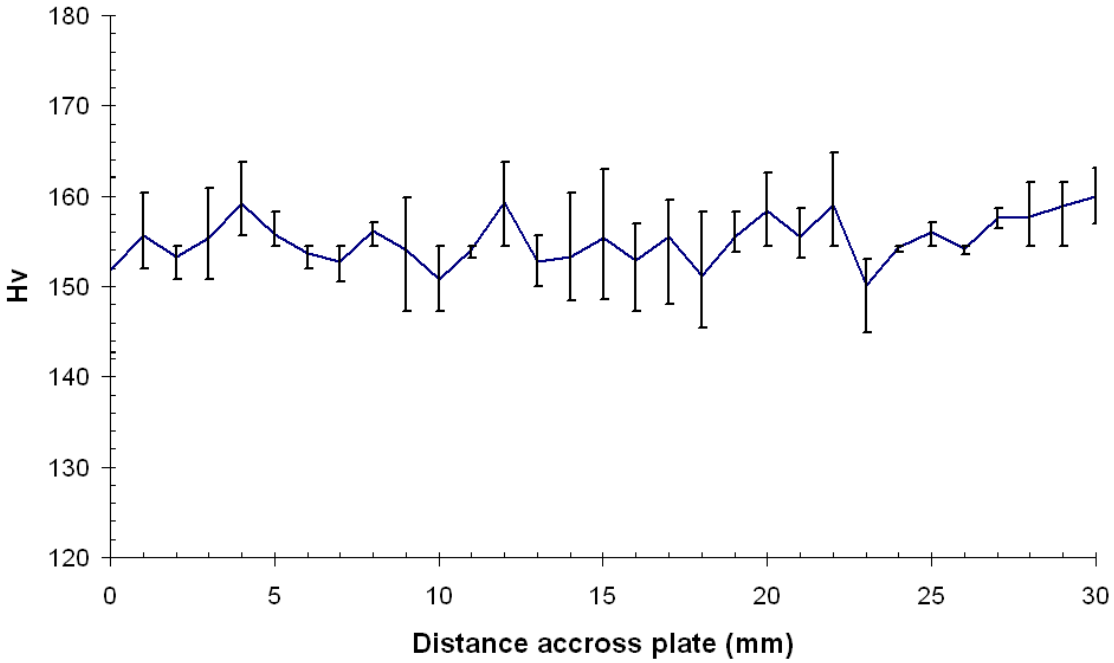


Figure 14. Mean average of three Vicker's micro hardness measurements taklen through the thickness of AA7017-T651 plate.

Compositional through thickness variation was also conducted using EDX and wavelength-dispersive X-ray spectroscopy (WDX); no variation was found using EDX, which is suitable for measuring the higher weight percentage alloying elements such as Zn and Mg (Figure 15). Three of the slowest diffusing lower weight percentage alloying elements, Mn, Cr and Zr, were then tested at different points through the plate using WDX. Slowest diffusing as these would be the most likely segregated. WDX of these elements also showed no significant variation, see Figure 16.

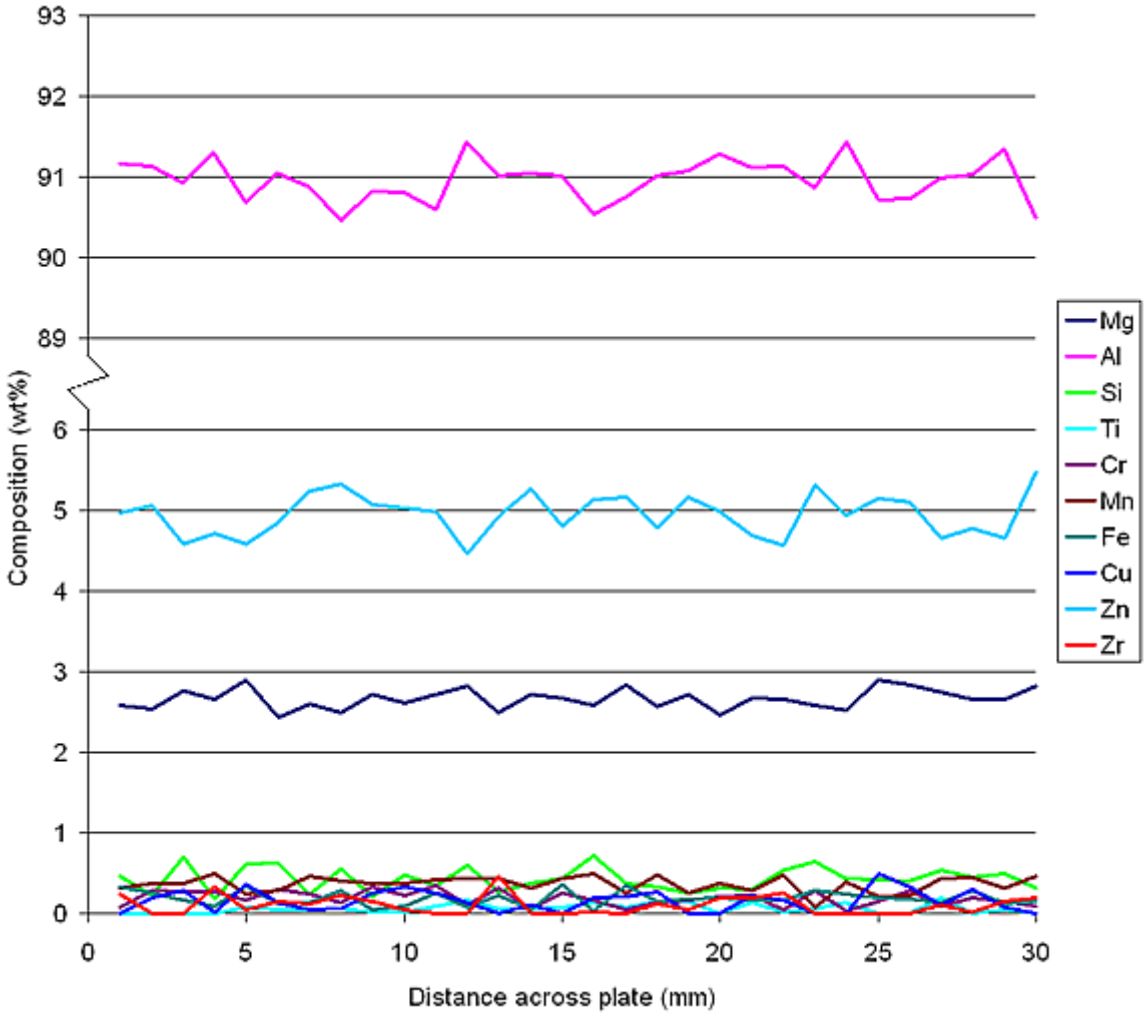


Figure 15. Composition of alloying elements in AA7017-T651 as measured by EDX at 1 mm intervals across the thickness of the plate.

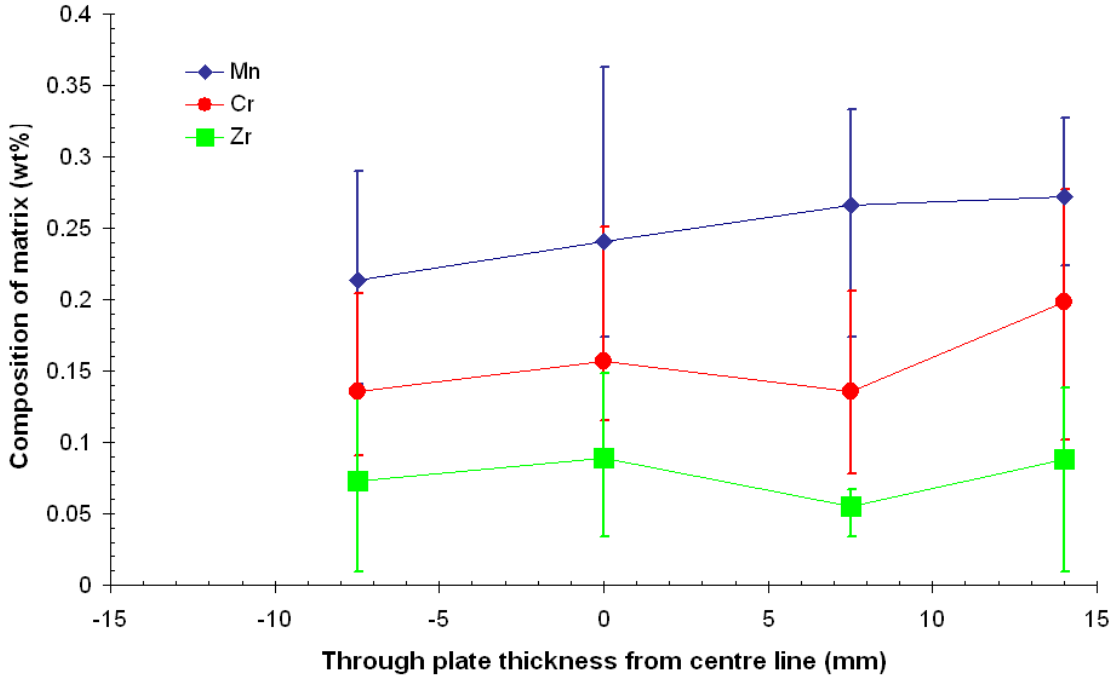


Figure 16. WDX measurements of the matrix composition of Mn, Cr and Zr at different depths within a sample of AA7017-T65151 plate. Error bars indicate the range of 5 repeat measurements taken at each depth.

4.2.3 Coarse Intermetallic Particle Identification

A SEM equipped with EDX was used to identify the coarse intermetallic particles present in the alloy. Figure 17 and Figure 18 show the general distribution of the coarse intermetallic particles. The sizes of the particles was in the region of 1-40 µm and so were often too small avoid signal contamination from the matrix surrounding them. Therefore analysis of large numbers of particles was conducted and then plotted to find the trend in their composition (Figure 19, Figure 20 & Figure 21). Fifty point analysis measurements were made for each type of particle. Three types of particle were identified.

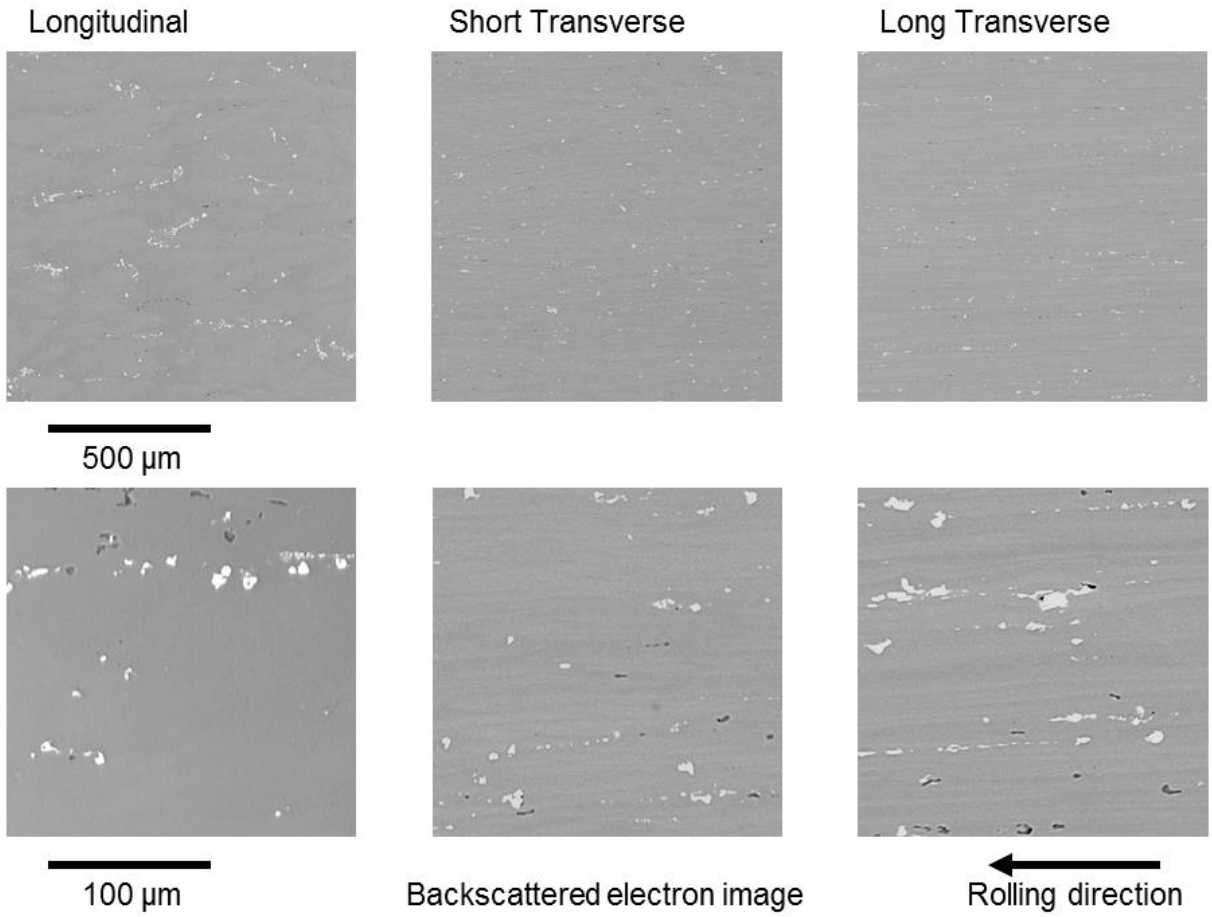


Figure 17. SEM backscatter images depicting representative distributions of coarse intermetallic particles in AA7017-T651 in three orthogonal directions at two magnifications.

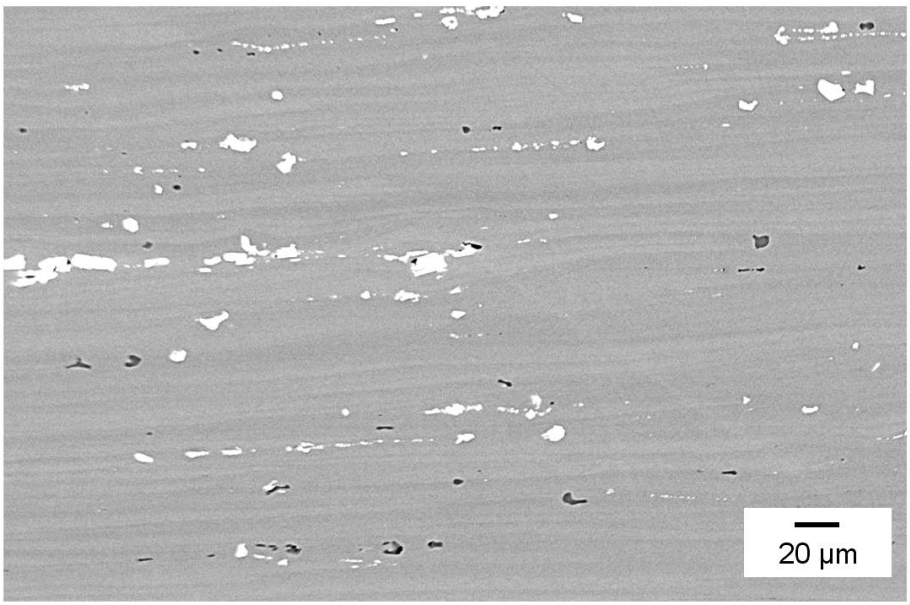


Figure 18. SEM backscatter image of the long transverse section of AA7017-T651 showing general distribution of coarse intermetallic particles.

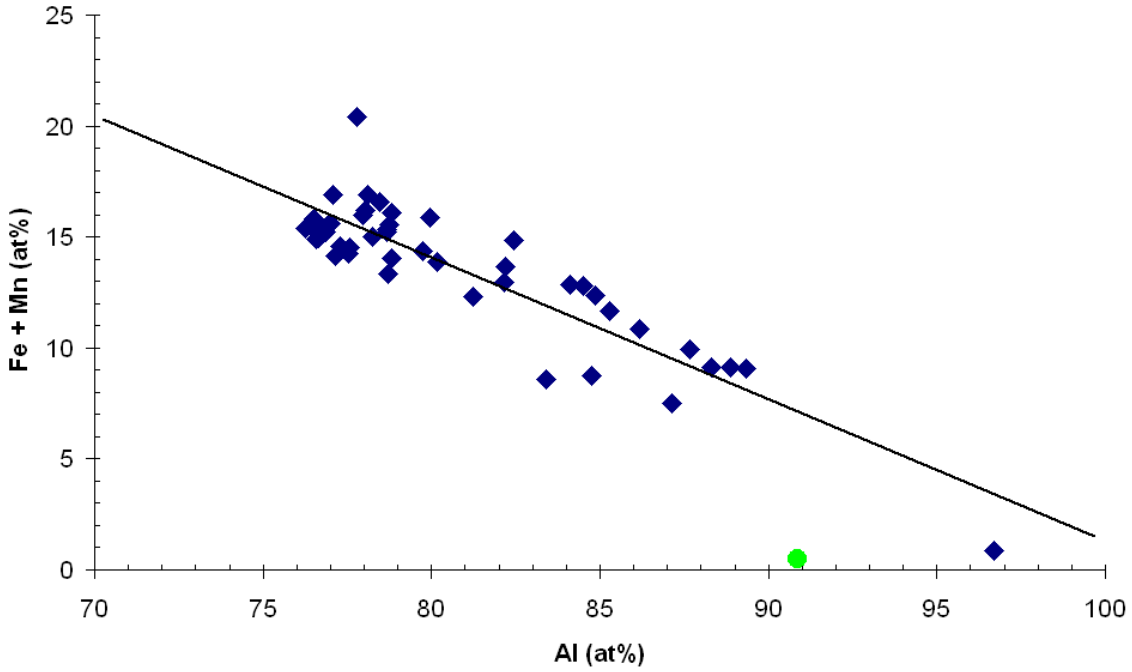


Figure 19. Scatter plot showing composition of Al verses the composition of all other elements present in Al_6(Fe, Mn) containing particles. The composition was determined using point analysis EDX. The green point shows the background composition of these elements.

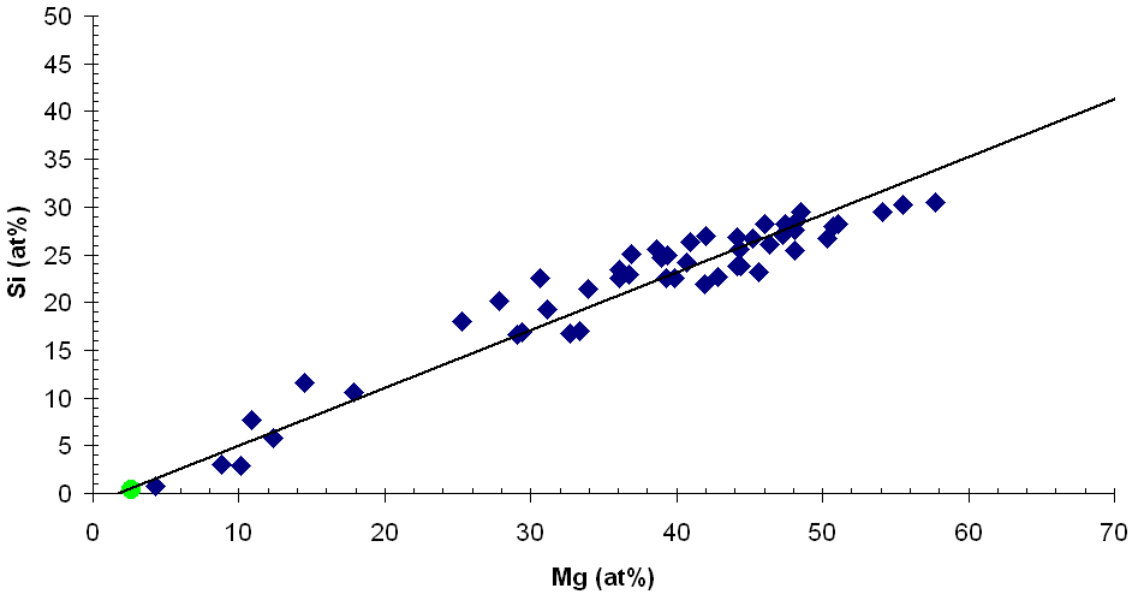


Figure 20. Scatter plot showing composition of Si verses Mg present in Mg_2Si containing particles. The composition was determined using point analysis EDX. The green point shows the background composition of these elements.

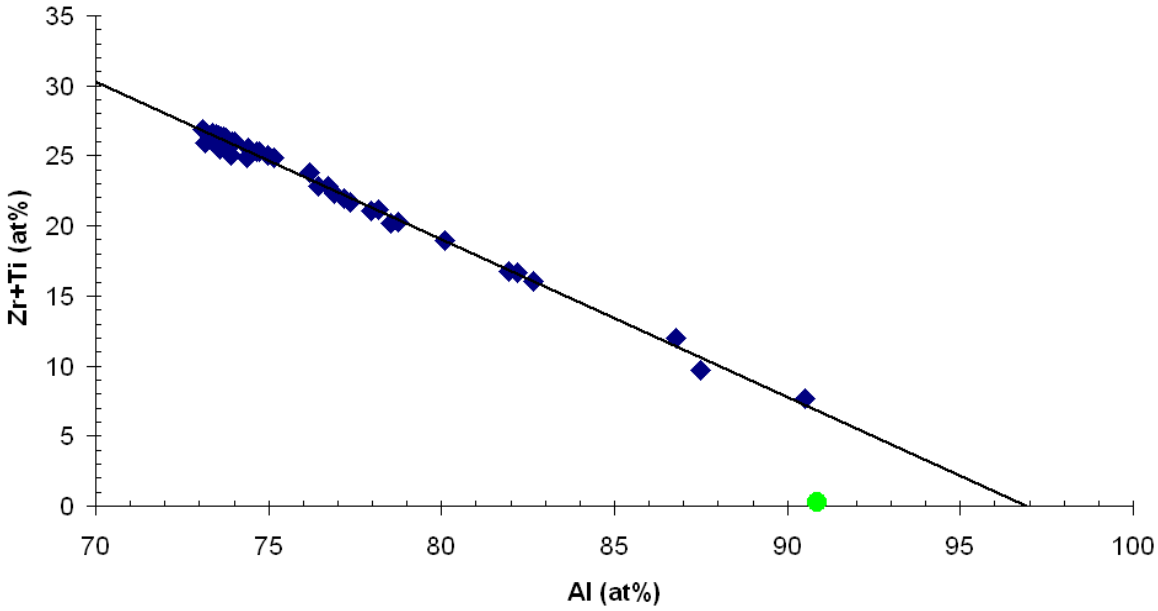


Figure 21. Scatter plot showing composition of Al verses Zr + Ti present in $Al_3(Zr, Ti)$ containing particles. The composition was determined using point analysis EDX. The green point shows the background composition of these elements.

Al_6(Fe, Mn) particles

Figure 22 shows the typical morphology of the Al_6(Fe, Mn) constituents found in this alloy. These constituents were typically found in clusters generally aligned in the rolling direction of the plate. The shape of the individual particles was random, but fairly angular with a wide variation in size, from 2-20µm. The number of Al_6(Fe, Mn) particles were counted and found to be ~650 per mm^2 ± 100. The silicon content of these particles was regularly ~5 at% or greater.

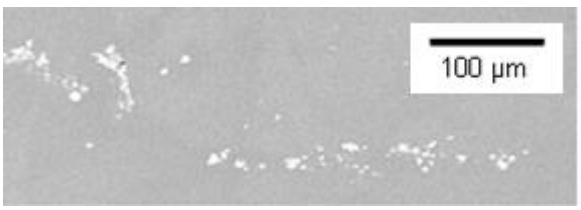


Figure 22. Backscattered Scanning Electron Microscope (SEM) image of AA7017- T651 in longitudinal section. Al_6(Fe, Mn) particles can be seen in white.

Mg_2Si particles

The dark particles in Figure 23 show the typical morphology of the Mg_2Si particles. They are generally found in small clusters containing 1-5 discrete particles. These particles are typically more rounded in shape than the other two constituent particle types, but can be found in groups of particles apparently fractured from one single particle. They are typically 1-20 µm in size. The number of Mg_2Si particles were counted and found to be ~110 per mm^2 +/- 30.

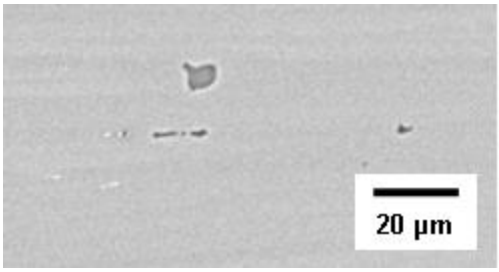


Figure 23. Backscattered Scanning Electron Microscope (SEM) image of AA7017 – T651 in longitudinal section. The dark particles are Mg_2Si.

Al_3(Zr, Ti) particles

By far the least common particle type are the Al_3(Zr, Ti) constituents, typically ~1.5 per mm^2 ± 1 of sectioned material. These are found in small clusters of highly angular plate like particles or fractured plate like particles. The plates are typically 5-10 µm in width and <40 µm in length, Figure 24 shows a typical example. Point EDX showed the composition of Zr to be ~20 at% ±1% and the composition of Ti ~5 at% ± 1%. Fortier et al. also found these particles to be present in AA7046 an alloy of similar composition to AA7017-T651 (17). Zr is added to these alloys to act as a grain refiner and retard recrystallization through forming fine dispersoids of Al_3Zr, however these particles are far too large in size to be performing this role. It is expected that these particles have formed in solidification and have been partially broken up during rolling.



Figure 24. Backscattered Scanning Electron Microscope (SEM) image of AA7017- T651 in longitudinal section. Al_3(Zr, Ti) particles can be seen in white.

4.3 Corrosion Characterisation

4.3.1 Sort Term Exposure to High Cl^- Concentration Solution

Figure 25 shows images of the three known particles found in AA7017-T651 before and after exposure to 5 wt% NaCl aerated solution (~1 M) at room temperature for 90 minutes. Multiple (<10) particles were examined before and after using point id EDX analysis on one sample and these particles were chosen at random for inclusion in this thesis. The Mg_2Si particles had a marked drop in Mg concentration upon point analysis with EDX, however Si concentrations generally stayed the same or only slightly lower. The sites where the Mg_2Si particles were identified generally resembled a void under secondary electron SEM observation. These observations would be consistent with anodic dissolution of the particles and/or the dealloying of the particles of Mg, leaving behind a Si rich remnant.

Both the Al_6(Fe, Mn) and Al_3(Zr, Ti) particles display cathodic grooving around their circumference. This is typical of cathodic activity as the local drop in pH causes instability of the passive film and the dissolution of the local matrix material. The grooving around some of the particles was not uniform on all sides, this can be seen in the image of the Al_3(Zr, Ti). There are two possible reasons for this:

1. There are marked inhomogeneities in the composition of the particle/matrix which make certain areas more cathodic than others, or

2. The test was so rapid that there was not time for the groove to grow to all sides of the particle, as there will always be minor inhomogeneities in the particle composition that will allow cathodic activity to begin in one place first over another.

It is also possible that grooving in those areas of the particles could be enhanced by the geometry of the particle, causing increased cathodic activity or occlusion for the concentration of low pH. Due to the resolution limits in EDX technique, it is not possible to identify any compositional variation in the particles.

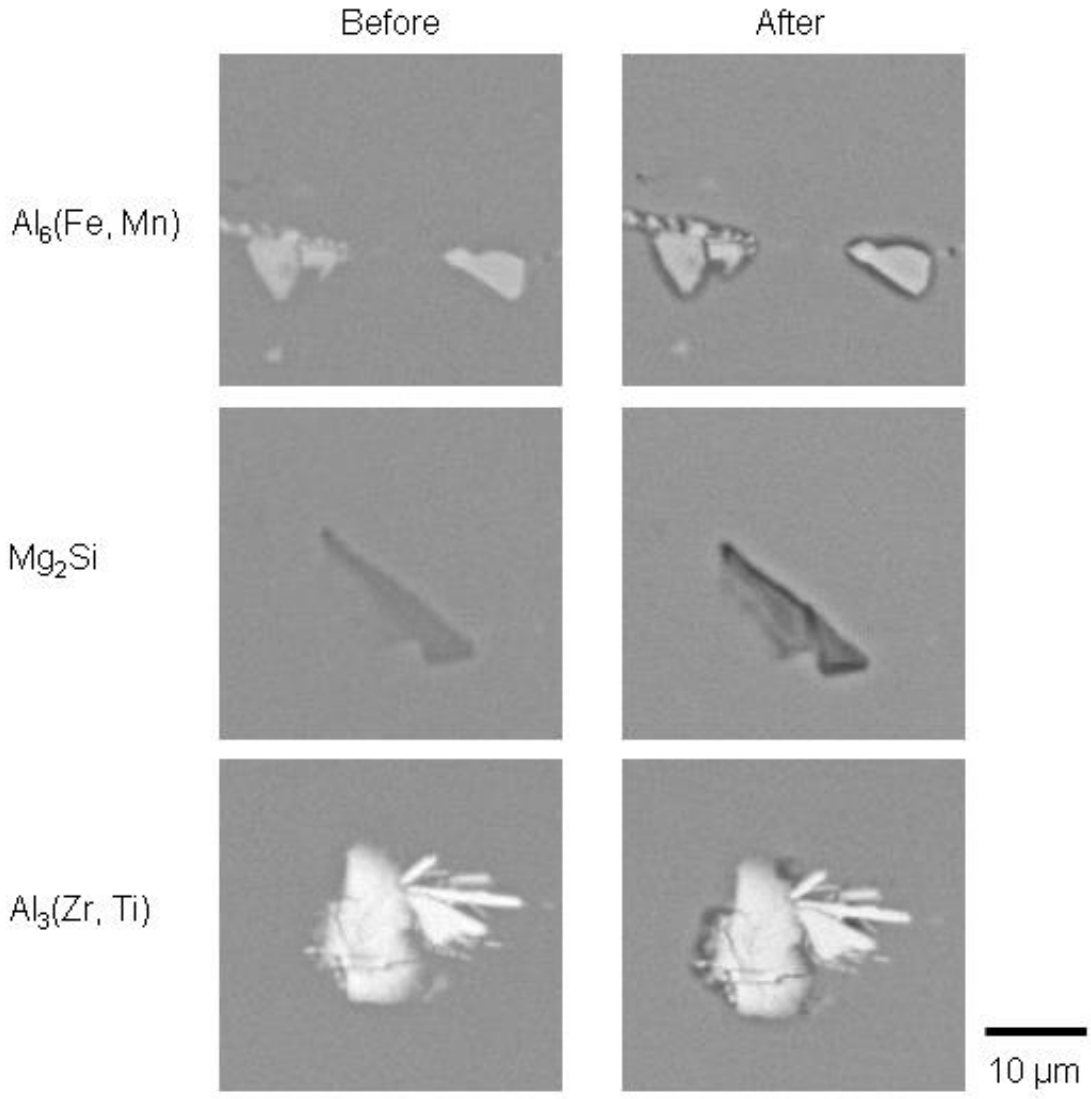


Figure 25. Before and after SEM backscattered electron images of the three particle types found in AA7017-T651 in longitudinal section. Showing before and after immersion in 5wt% NaCl solution for 90 min at room temperature.

4.3.2 Longer Exposure to Lower Cl^- Concentration solution

In this test polished samples were exposed to 0.1 M NaCl solution at room temperature for initially 16 hours (Figure 26) which showed little attack except around the cathodically active particles. Therefore a longer duration of 40 hours was chosen for further testing. The three orthogonal sections after immersion can be seen in Figure 27, it can be noted that the surface discolouration in the longitudinal direction is different to that of the longitudinal transverse and the short transverse. The long transverse section after immersion is shown in Figure 28, corrosion product can be seen around the Al_6(Fe, Mn) and Al_3(Zr, Ti) particles but not the Mg_2Si particles. Unknown surface deposits were seen and are indicated by white arrows, these deposits were ubiquitous and not apparently associated with any microstructural features. EDX analysis could not find any measurable chemical identity to these deposits; this could be due to the lack of a great enough interaction volume, the composition being the same as the bulk matrix, or due to them being formed substantially of the lighter elements undetectable by EDX.

The samples were then cleaned of corrosion product by immersing in concentrated nitric acid for 20s. Figure 29 shows an SEM image of the surface at 30° to the normal. It can be seen that after this time cathodic grooving has progressed to such an extent as to undermine the Al_6(Fe, Mn) coarse intermetallics, which have then subsequently fallen out of the surface. This also occurs with the Si rich remnants of the Mg_2Si particles.

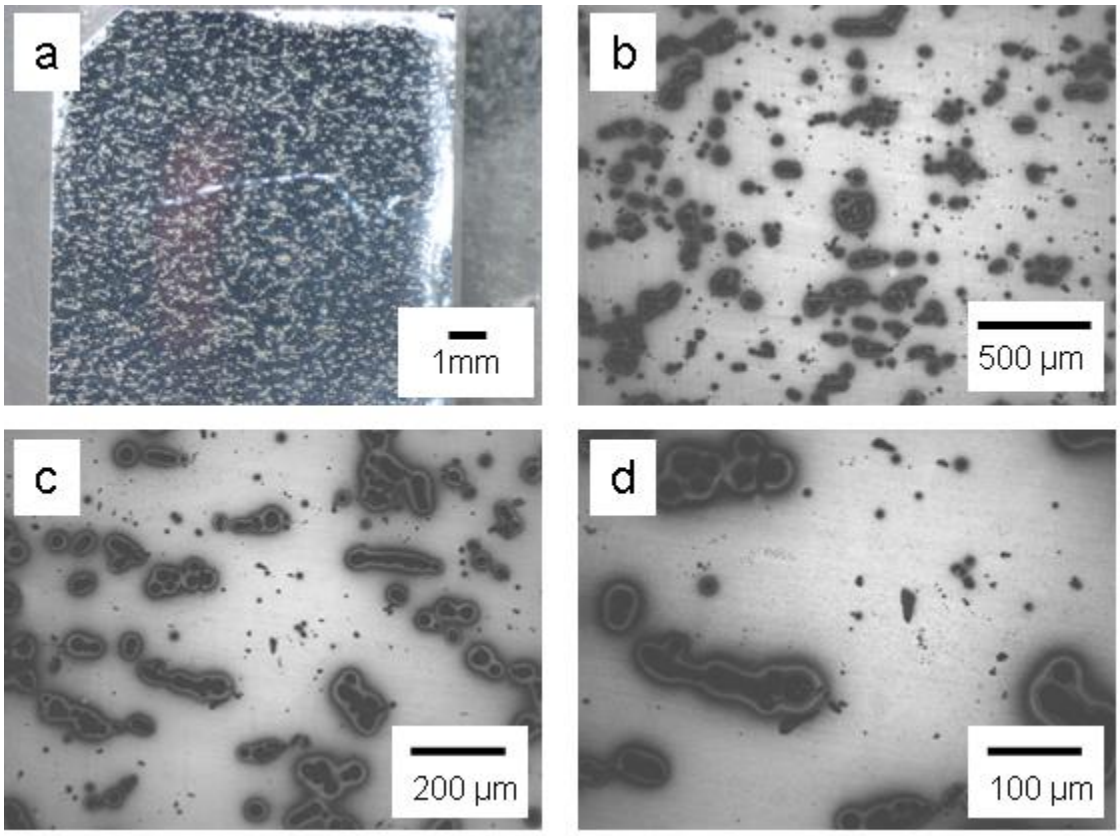


Figure 26. Microscope images of polished longitudinal face of AA7017-T651 after immersion in 0.1 M NaCl solution for 16 hours at room temperature. Various magnifications are shown and labelled.

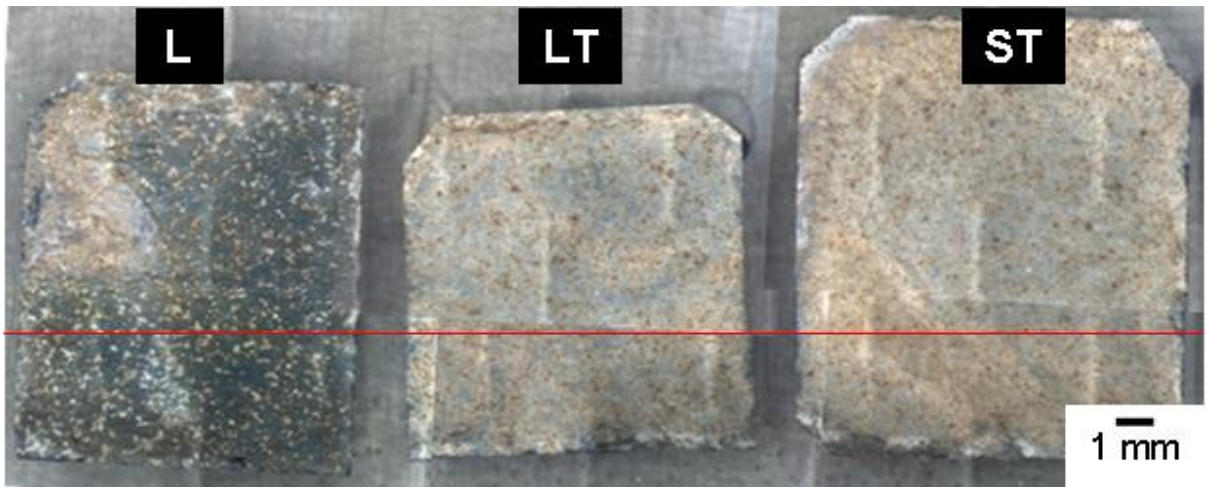


Figure 27. Stitched microscope images of three orthogonal faces of AA7017-T651 after exposure to 0.1 M NaCl solution for 40 hours. Longitudinal face (L), long transverse (LT) face and short transverse (ST) sections are labelled. Red line indicates where samples were sectioned.

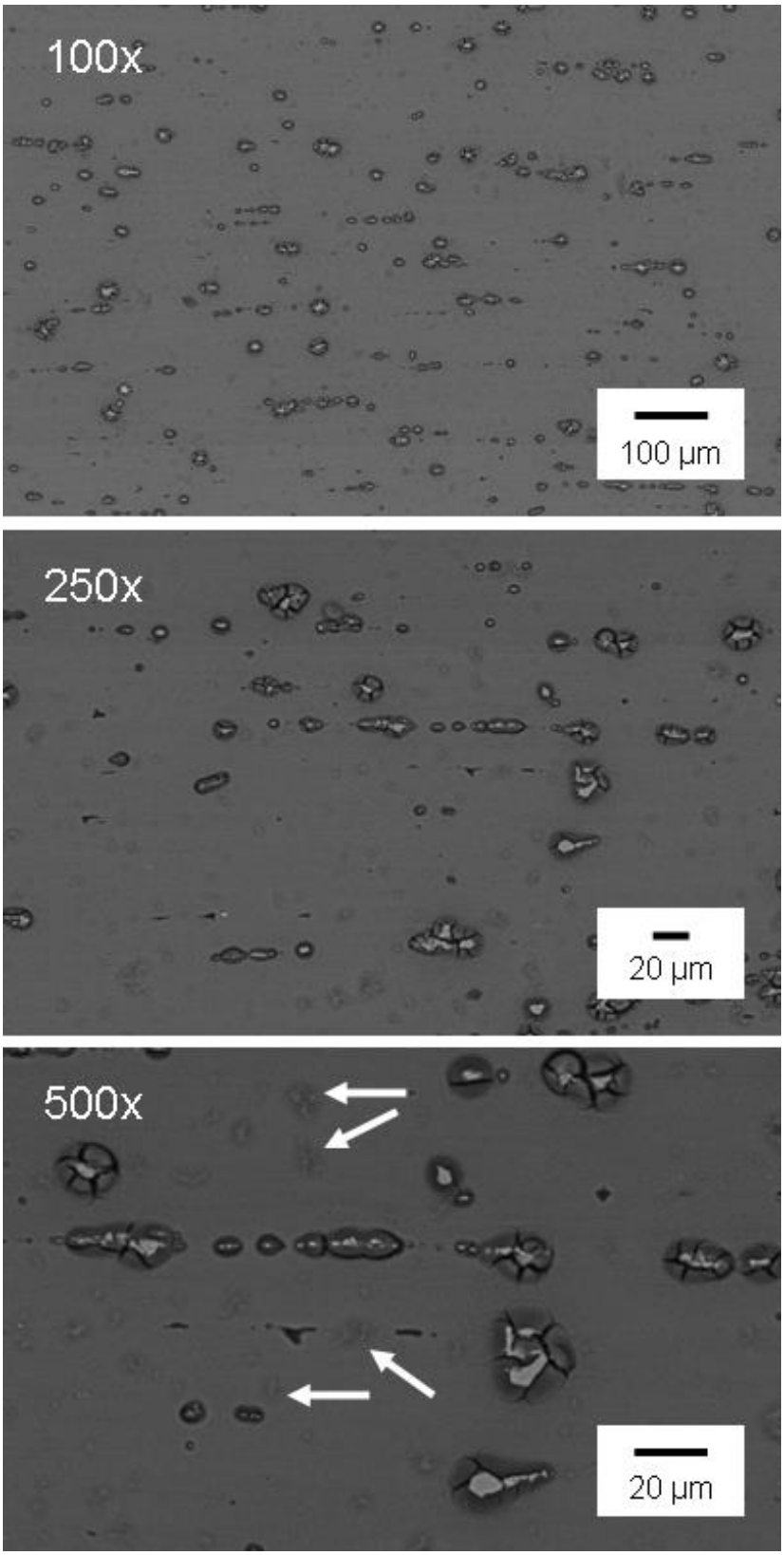


Figure 28. SEM backscattered electron images of long transverse section of AA7017-T651 after 40 hours immersion in 0.1 M NaCl solution at room temperature. Three magnifications are given and are labelled, 100x, 250x and 500x. White arrows indicate unknown surface deposits.

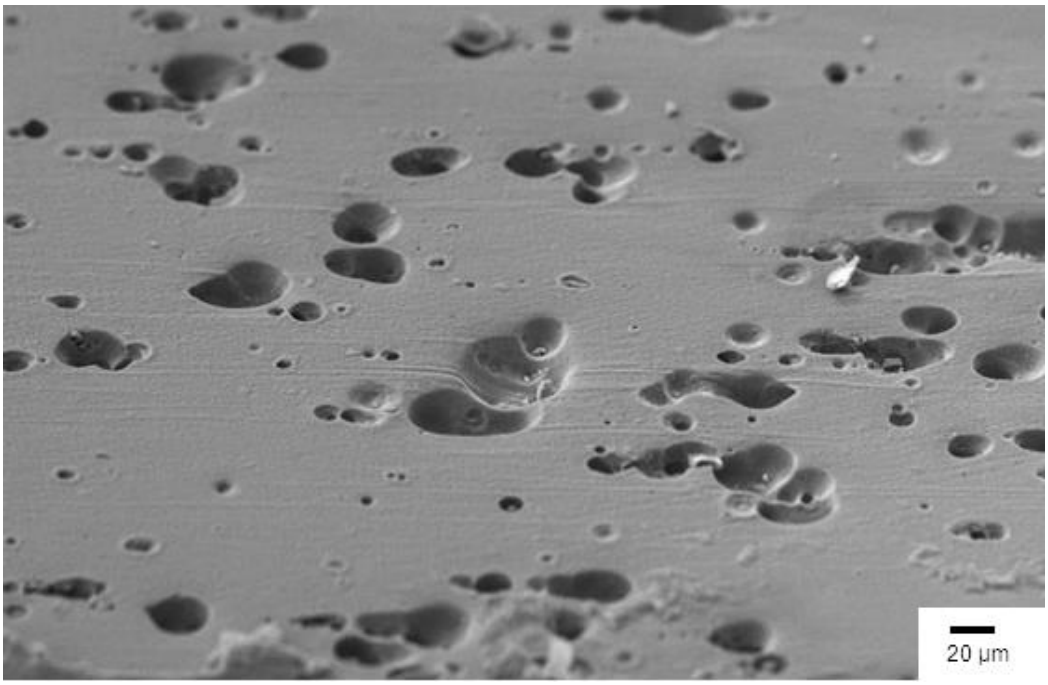


Figure 29. SEM micrograph taken at 30° from the normal, depicting the surface of a AA7017-T651 sample in longitudinal section after exposure to a 0.1 M NaCl solution at room temperature for 40 hours, nitric acid cleaned.

Figure 30 shows image of the surface at 30° to the normal of the same sample as in Figure 29. These are images representative of the $Al_3(Zr, Ti)$ coarse intermetallics. They also show cathodic grooving however the particles are large enough to remain embedded in the surface after this length of exposure.

Figure 31 is of the same sample as depicted in Figure 29 and Figure 30. It shows the morphology of the cathodic grove interiors. The cathodic grooving is typically shallow and open. This form of attack would not lead to the occluded environment required for sustained localised attack. As the solution surrounding the pit is free to diffuse into the grove and neutralise any acidity caused by later anodic activity within the grove. The same goes for the increased concentration of Cl^- ions within a pit typical of localised corrosion.

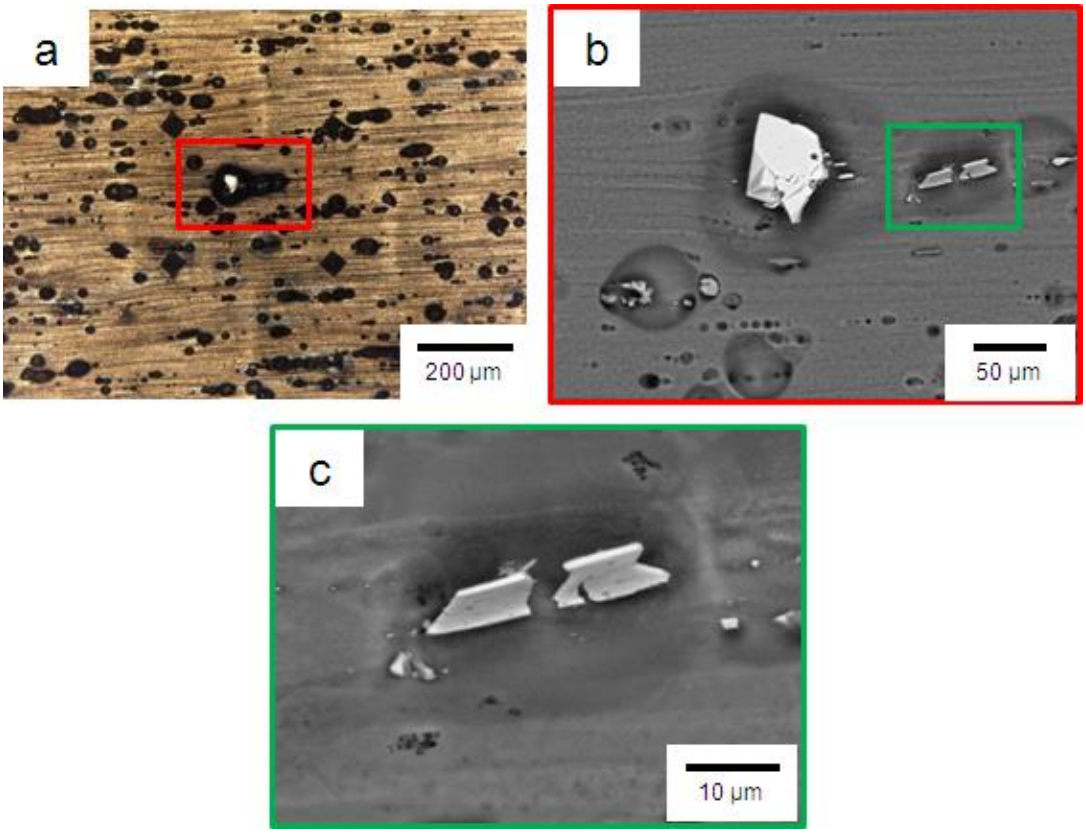


Figure 30. Images of increasing magnification depicting a AA7017-T651 surface in longitudinal section after exposure to a 0.1 M NaCl solution for 40 hours. a) Optical micrograph showing a Al_3(Zr, Ti) coarse intermetallic at the centre. b) and c) SEM micrographs taken at increasing magnifications of the same intermetallic.

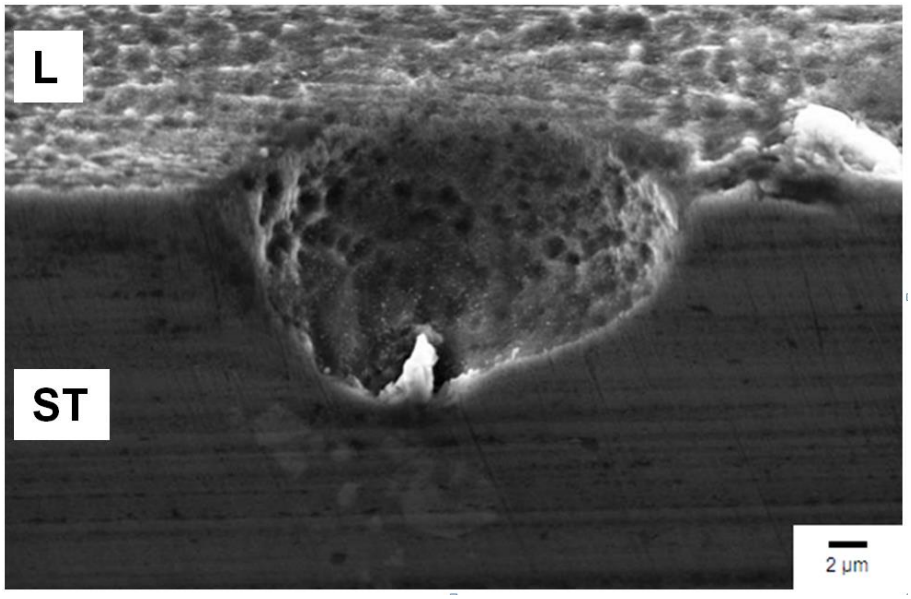


Figure 31. Cross section SEM micrograph taken at 30° from the normal to the longitudinal (L) section of sample shown in Figure 29, depicting the surface of a AA7017-T651 sample after exposure to a 0.1 M NaCl solution at room temperature for 40 hours, short transverse plane labelled (ST).

4.3.3 Electrochemistry

4.3.3.1 Anodic Polarisation

Anodic polarisation measurements were made of AA7017-T651, these are plotted in Figure 32 along with the curves taken from Meng (19). They show that AA7017-T651 has two breakdown potentials, E_1 and E_2, similar to that found by Meng for other Cu containing 7xxx series alloys (19). AA7017-T651 fits with the pattern observed by Meng (19), in that Cu content will dictate the corrosion potential of the material. E_1 for AA7017-T651 being -840 mV (Ag/AgCl) and E_2 being -760 mV (Ag/AgCl), where , E_1 is associated with the dissolution of an active surface layer and, E_2 is the actual breakdown potential of the bulk material.

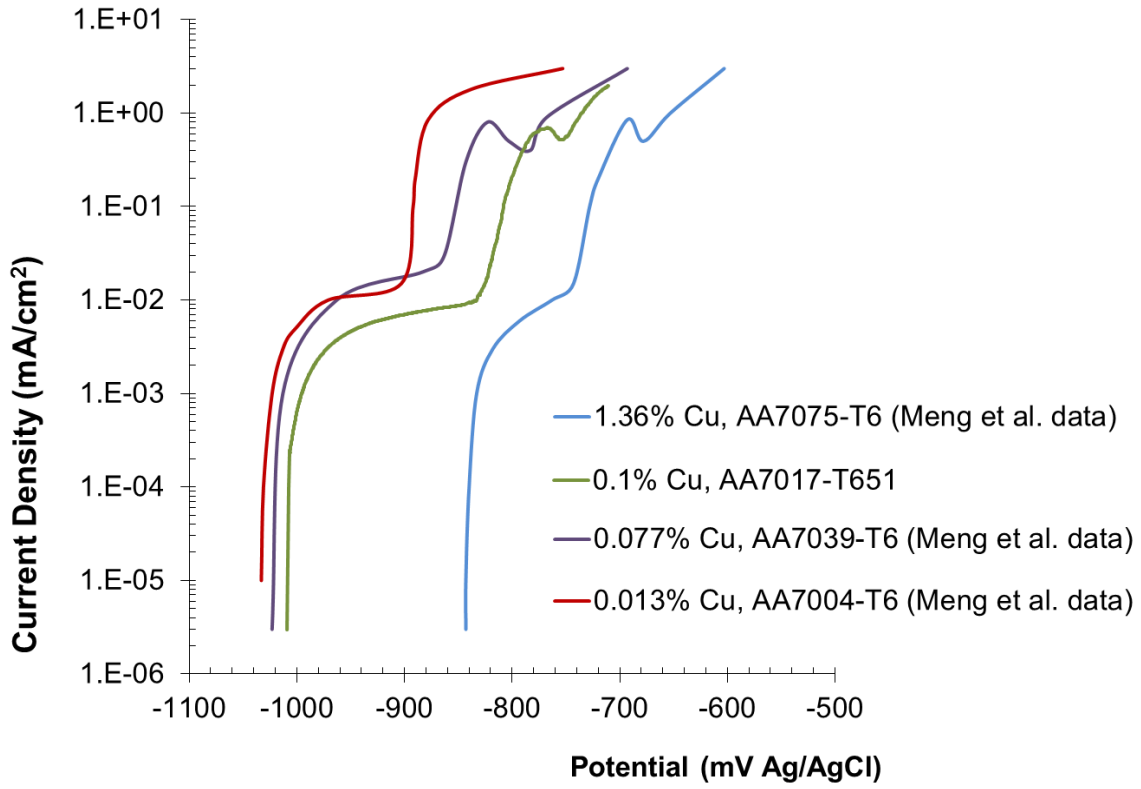


Figure 32. Anodic polarisation curves for AA7017-T651, AA7039-T6 and AA7017-T651 in deaerated 0.5 M NaCl, pH 3.56 with a scan rate of 0.2 mV/s. (Dashed lines are taken from data from Meng (19).)

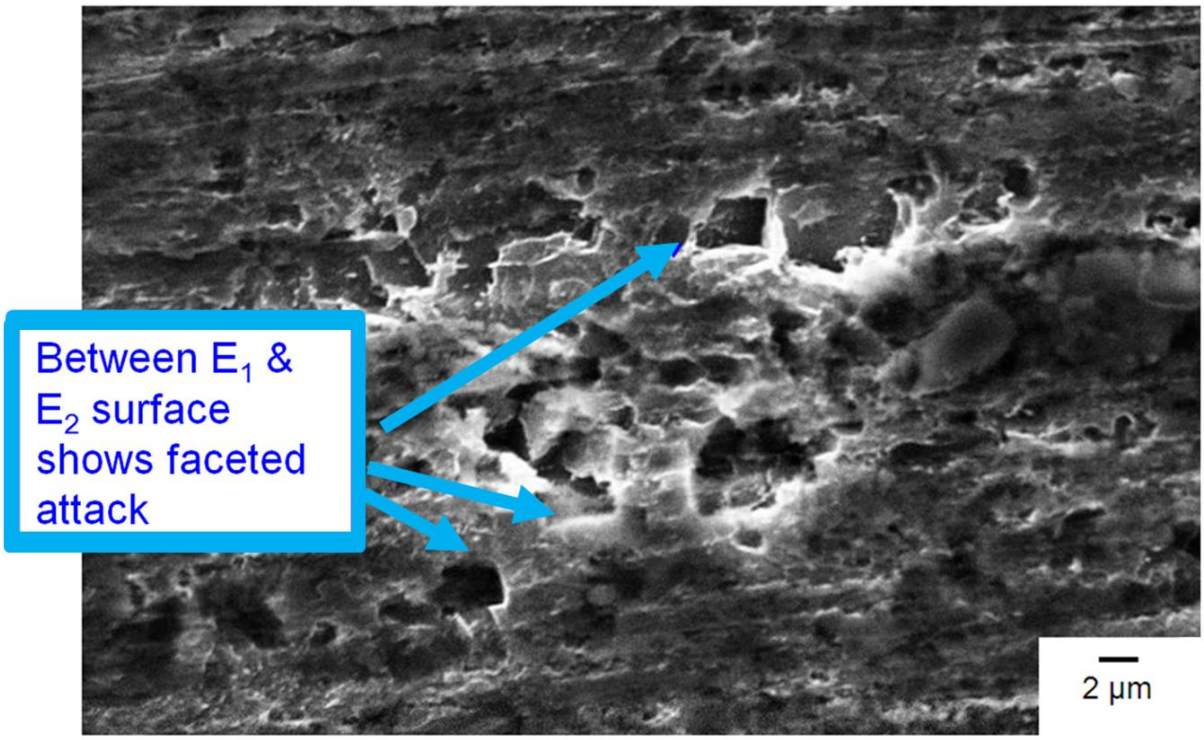


Figure 33. SEM image of AA7017-T651 in the short transverse section surface after polarisation beyond the E_1 breakdown potential.

Between E_1 and E_2 the morphology of the surface attack found was as shown above in Figure 33. The surface showed angular facets where material had been removed through corrosion. These features are on the scale of sub-grains and so it is thought they indicate selective sub-grain attack and dissolution beyond the first breakdown potential of the material.

4.3.3.2 Open Circuit Conditions

Figure 34 shows the open circuit potential of AA7017-T651 over the initial 1000 seconds of exposure, compared to the values by Meng et al. for three other 7xxx series alloys (19). The rest potential of AA7017-T651 is consistent with the findings of Meng et al., that increasing Cu content influences the open circuit behaviour negatively (19). The open circuit potential for AA7017-T651 is close to that of AA7039, which has a similar Cu content and fits the pattern of increased Cu content relating to increased corrosion potential. This suggests that Cu content also dominates the corrosion potential of AA7017-T651 over the transient initial corrosion of the modified surface layer.

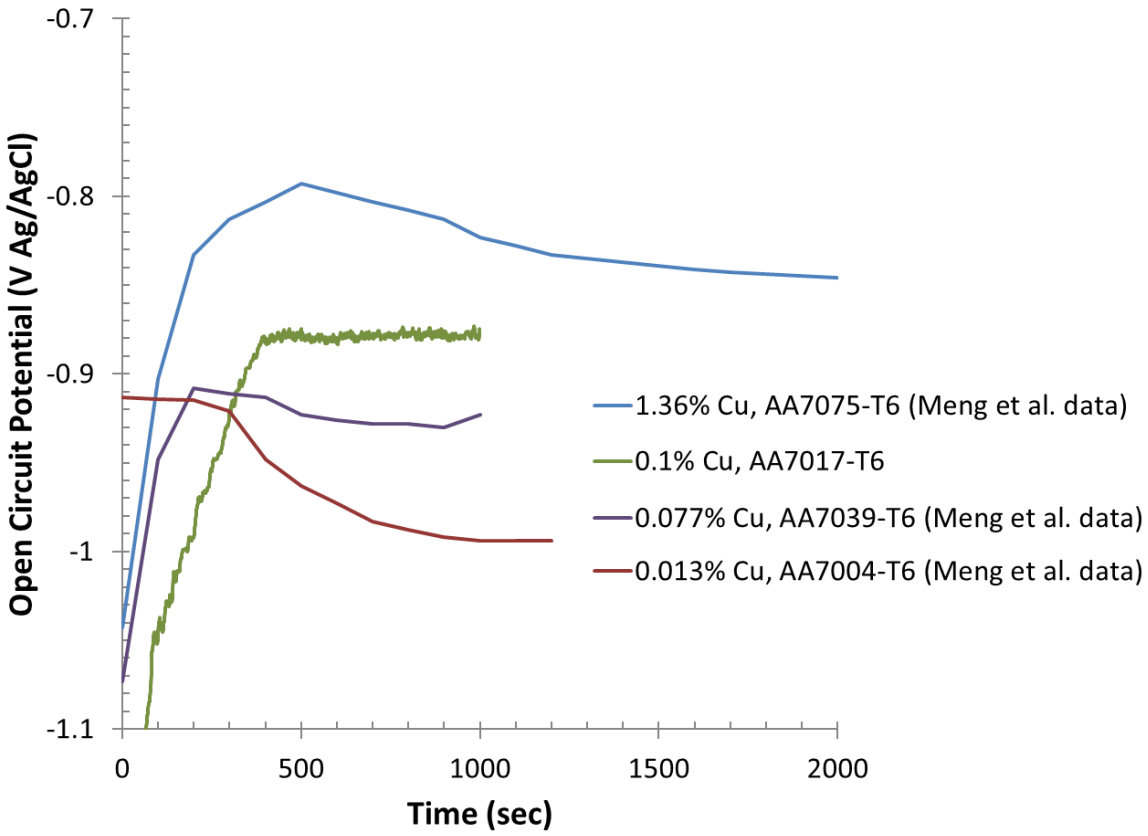


Figure 34. Open circuit potential measurements of initial exposure of AA7017-T651 to deaerated 0.5 M NaCl solution adjusted to pH 3.56, compared with data from Meng et al. under the same conditions. (19)

Longer term open circuit measurements were taken under the same conditions. These are shown in Figure 35, which also plots the results found by Meng (19). It can be seen that for the first 48 hours AA7017-T651 behaves similarly to the alloy of similar Cu content AA7039-T6. Meng states that an alloy of this low Cu content cannot sustain localised corrosion and so as seen in Figure 35, the OCP drops to a very low value (-1050 mV). Figure 35 shows that AA7017-T651 maintains a high OCP value over the entire week; this suggests that AA7017-T651 is more susceptible to free corrosion than AA7039-T6. The form of attack on the surface of the long term open circuit samples can be seen in the SEM image in Figure 36. This shows suspected selective sub-grain attack very similar to that shown beyond the E_2 breakdown potential as see in Figure 33, which is supported by the OCP shown in Figure 35 being between the E_1 and E_2 potentials.

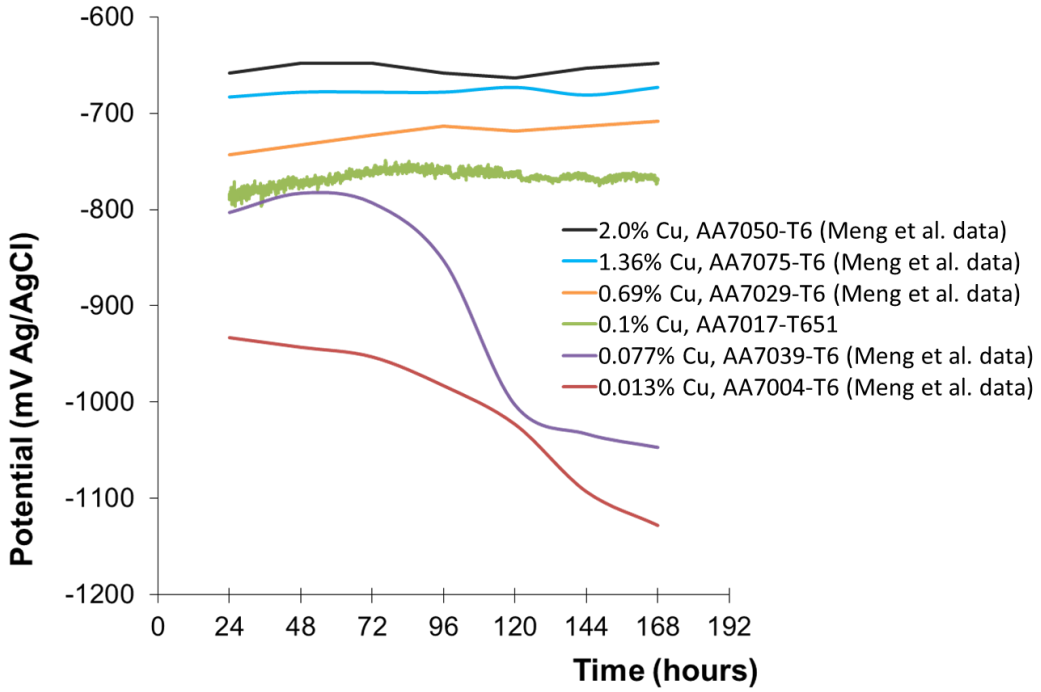


Figure 35. Long term open circuit potential measurements of a AA7017-T651 sample exposed to 0.5 M NaCl solution pH adjusted to 3.56, at room temperature and open to the air, plotted against Meng et al. data. (19)

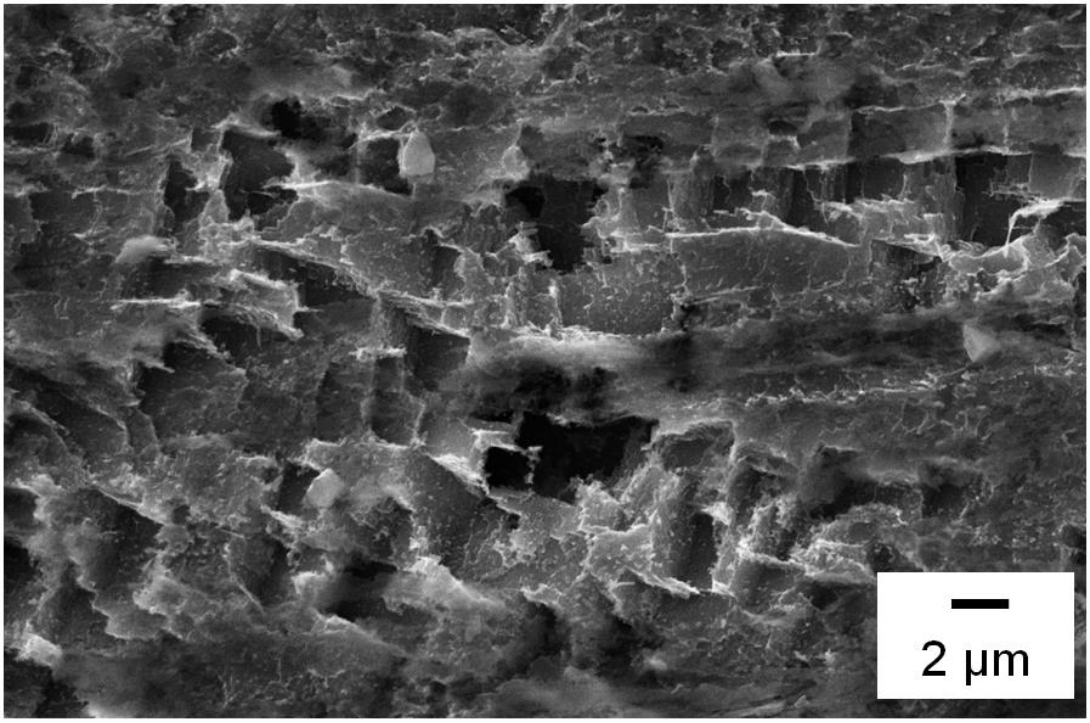


Figure 36. Secondary electron image of the surface of a sample of AA7017-T651 in the short transverse section exposed to 0.5 M NaCl solution pH adjusted to 3.56 for 336 hours.

4.3.4 Discussion

As covered in the literature review, it has been shown that the nature of the intermetallic particles found in an alloy can have a strong influence on the corrosion characteristics. With this in mind microstructural characterisation was conducted. Point EDX has shown that this alloy contains three coarse intermetallic particles, Al_6(Fe, Mn), Mg_2Si and Al_3(Zr, Ti). This tells us that the Cu levels were not sufficient for Cu containing coarse intermetallic particles to develop. This is important as Cu containing intermetallics are suspected to lead to Cu enrichment on the surface, eventually leading to localised corrosion.

Short exposures to high chloride concentration aerated solution gave an indication as to the electrochemical nature of the coarse intermetallics. The Al_6(Fe, Mn) and Al_3(Zr, Ti) particles displayed cathodic grooving in the surrounding matrix and stayed intact after

exposure, meaning they are likely noble relative to the matrix. Whereas the Mg_2Si constituent particles were found to leave what appeared to be a void in the surface after exposure. EDX analysis of the location previously occupied by the Mg_2Si particles showed a strong Si signal. This is most likely due to Mg dealloying from the particle leaving a Si rich sponge remnant as has been observed by others (67, 69-74). None of the samples showed signs pitting or IGC at either the cathodic or anodic particle sites.

Long term exposure to a less concentrated aerated salt solution of 40 hours was conducted to attempt to develop some sustained localised corrosion. Visual inspection of both the surface and cross-sections in all three orthogonal directions showed no evidence of pitting or IGC at any point on the surface including the coarse intermetallic particles. In most instances the Al_6(Fe, Mn) intermetallic particles had experienced such great cathodic grooving as to free the particle of the matrix. The far rarer Al_3Zr particles however remained imbedded in the surface, most likely due to their far greater size requiring a greater amount of alkaline attack to undermine them.

As it was found to be difficult to achieve substantial attack of the alloy, electrochemical investigations were conducted. It was suspected that Cu would play a key role in the corrosion behaviour the results were compared with those of Meng (15), where the measurement of a range of 7xxx series alloys of various Cu content was made. To make sure that the results obtained were accurately reproducing those gathered by Meng an AA7075-T6 sample was also tested in parallel and compared with his results for the same material (15).

In the as-polished state AA7017-T651 shows two breakdown potentials which follow the observations of others (19) and the mechanism proposed by of Zhijun (78). This is due to the presence of a modified surface layer formed on polishing. Meng et al. (19) showed a link between Cu content and the presence of this transient first breakdown, with the exception of the low copper alloy AA7004-T6 not demonstrating this behaviour. It was therefore chosen to establish if an active surface layer as was also present in AA7017. Figure 32 shows the results of Meng compared to those gathered for AA7017-T651 (19). It can be seen that AA7017-T651 fits where would be predicted for its Cu content and also displays the two distinct breakdown potentials, E_1 and E_2, consistent with the dissolution of an active surface layer followed by the breakdown potential of the bulk alloy. This gave confidence that Cu too plays a key role in the corrosion characteristics of this alloy.

Further confidence that the findings of Meng (19) were consistent with AA7017-T651 was found in the OCP of the first 1000 seconds of exposure to the solution, Figure 34. Here too the pattern of increased Cu content relating to increased corrosion potential is maintained. This suggests that Cu content also dominates the corrosion potential of AA7017-T651 under deaerated conditions.

Of most interest were the long term OCP measurements with aerated solution that show AA7017-T651 exhibits corrosion behaviour more akin to that of the high Cu content 7xxx series alloys. Figure 35 shows this relationship, where the initially high corrosion potentials of the low Cu AA7004-T6 and AA7039-T6 drop after several days to much lower potentials, whereas AA7017-T651 and the high copper non-weldable alloys maintain this high corrosion potential. Meng explains the relationship of increasing corrosion

potential with increasing Cu content as being connected through the Cu enrichment and redistribution theory (19). Stating that the sharp contrast in the sustained corrosion potential in the intermediate and high Cu alloys is likely the result of the enhanced oxygen reduction reactions associated with redistributed Cu on the surface. This does not however satisfactorily explain why there is such a dramatic difference between the low Cu alloys and the others and why the relationship is not linear. If Cu content is the major contributing factor in maintaining a high corrosion potential then the amount found in AA7017-T651 must be sufficient to redeposit on the surface to maintain the cathodic reduction reactions.

These findings however shed further light on the precise mechanism of Cu enrichment and redistribution as there is no Cu rich coarse intermetallics found in AA7017-T651. This means that only Cu dealloyed from the matrix would be able to be explained as present for enrichment and must be sufficient at the early stages of surface dissolution to maintain the high potentials initially achieved through the dissolution of the active surface layer.

Further work will need to be conducted to confirm the presence of enriched and redistributed Cu on the surface of AA7017-T651 through X-ray Photoelectron Spectroscopy (XPS).

Figure 36 shows the nature of attack after exposure to free corrosion condition of 2 weeks. There appears to be selective crystallographic attack of the subgrains. This is of interest in helping to characterise the nature of attack under free corrosion conditions. Even with a sustained corrosion potential close to that of the second breakdown potential for AA7017-T651 there was little localised corrosion found other than this subgrain attack. This

is contrary to the electrochemical data. Further work will be needed to explain these findings.

5 SUMMARY AND CONCLUSIONS

5.1 Summary and Conclusions

The focus of this work is the aluminium alloy AA7017-T651. It has a low Cu level of 0.2 wt% to aid with weldability. Cu levels in the 7xxx series alloys are of key importance to their corrosion behaviour and typically range from essentially Cu-free up to 2 wt%. Most work reported in the literature has focused on the high Cu alloys such as AA7075 where Cu enrichment and redistribution plays a key role in localised corrosion.

Although the Cu levels in AA7017-T651 are low in the 7xxx series they are some of the highest found in the weldable grades. OCP measurements were taken in aerated solutions to ascertain the corrosion behaviour of AA7017-T651 relative to the other 7xxx series alloys. Typically low Cu weldable 7xxx series alloys show an initially high OCP that corresponds to the dissolution of an active surface layer. The corrosion potential then drops after several days and little localised corrosion is found in these alloys. In high Cu 7xxx series alloys the corrosion potential is maintained at the initially high levels and this is due to Cu enrichment and redistribution leading to sustained localised corrosion. In this work it was found that AA7017-T651, although a weldable Cu alloy behaves in a similar manner to the high Cu 7xxx series alloys and maintains a high OCP after the dissolution of the active surface layer. It follows therefore that 0.2 wt% Cu is beyond that required for sustained localized corrosion in 7xxx series alloys, excluding any unknown contributing factors in AA7017-T651.

The microstructure of AA7017-T651 was also characterised as this information could not be found in the known literature. It was found that AA7017-T651 contained a fully non-recrystallized grain structure containing three main constituent particles. In order of prevalence, Al_6(Fe, Mn), Mg_2Si and Al_3(Zr, Ti) particles were found. As is found in other 7xxx series alloys the Mg_2Si constituents behaved anodically and the Al_6(Fe, Mn) and Al_3(Zr, Ti) constituents cathodically in relation to the matrix. These three types of particle were found to be uniformly spread throughout the plate when surveyed in the three orthogonal directions and had distinguishing distribution and morphology. Surprisingly none of the three types of intermetallic particles found in this alloy contain copper, which is identified as the key contributing factor in sustained higher corrosion potentials in higher copper 7xxx series alloys which display copper enrichment and redistribution (section 2.2.3.3.). The mechanism by which this is occurring should be the subject of further work.

6 APPENDIX

6.1 Experiments in developing AA7017-T651 using Keller's reagent

Figure A1 shows progressively longer exposure of AA7017-T651 to Keller's reagent in order to ascertain the optimum etch time and develop clear grain boundaries. Clear grain boundaries could not be developed due to the non-recrystralised microstructure.

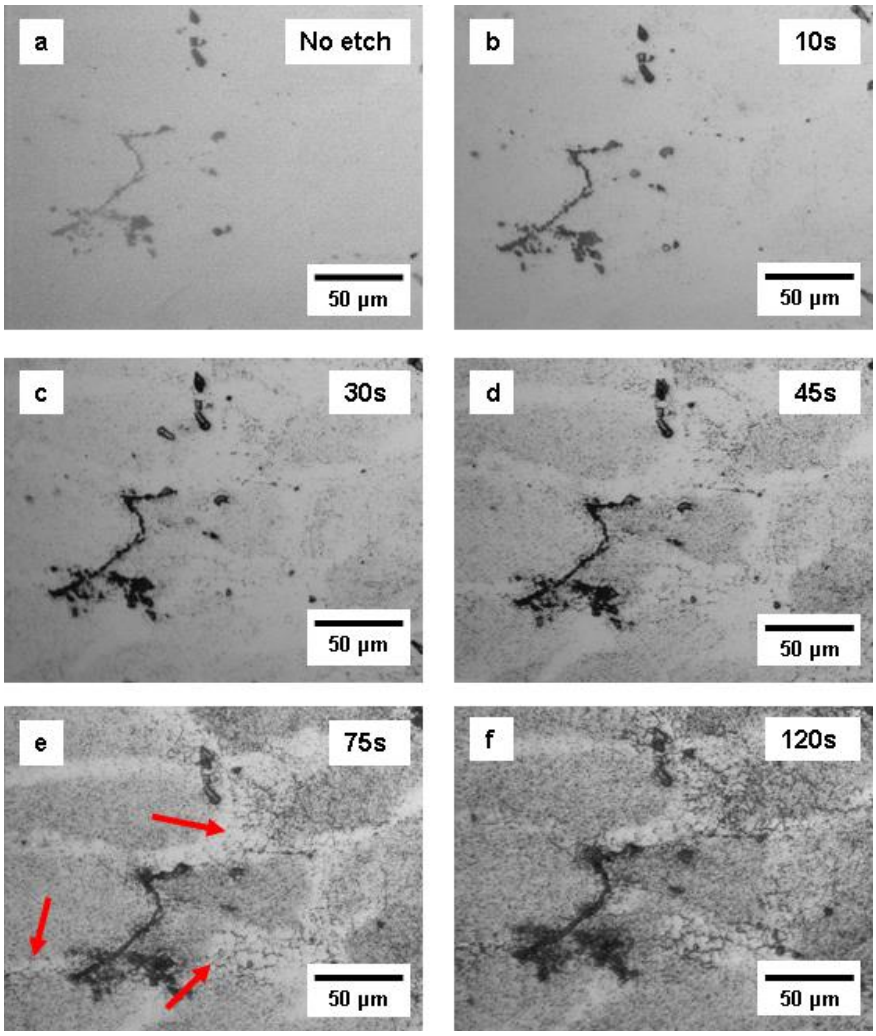


Figure A1. Microstructure of AA7017-T651 in longitudinal section after being etched in Keller's reagent for varying amounts of time, (a) No etch (as polished), (b) 10s etch, (c) 30s etch, (d) 45s etch, (e) 75s etch, (f) 120s etch.

7 REFERENCES

1. IADS. Online Teal Sheets: Aluminium Association of America; 2010.
2. M. R. Clinch SJH, W. Hepples, N. J. H. Holroyd, M.J. Lawday, B. Noble, editor. Optimising the Mechanical Properties of 7XXX Series Alloys by Controlling Composition and Precipitation Kinetics. 11th International Conference on Aluminium Alloys; 2008; Aachen, Germany: Wiley-VCH.
3. Metals Handbook, Heat Treating. 9th ed: ASM International; 1981.
4. Aluminium Company of America. Alcoa Aluminium Handbook. Pittsburgh, PA.
5. The Aluminium Association tE. Standards for Aluminium Mill Products. N.Y.1966.
6. Yoon Y, Buchheit RG. The effect of Cu content on chromate conversion coating formation of compositional analogs of the eta phase Mg(Zn,xCu)(2). Electrochemical and Solid State Letters. 2005;8(11):B65-B8.
7. G. Bergmann LTW, L. Paulng. Acta Cryst. 1957;10:254.
8. Starke Jr. EA. Concise Encyclopedia of: The Structure of Materials. 1st ed. Martin JW, editor: Elsevier; 2007.
9. Polmear I. Light Alloys - From Traditional Alloys to Nanocrystals. 4th ed: Butterworth-Heinemann; 2007.
10. Mukhopadhyay AK. Microstructure and Properties of High Strength Aluminium Alloys for Structural Applications. Transactions of The Indian Institute of Metals. 2009;62(2):113-22.

11. Sarkar B, Marek M, Starke E. The effect of copper content and heat treatment on the stress corrosion characteristics of Ai-6Zn-2Mg-X Cu alloys. Metallurgical and Materials Transactions A. 1981;12(11):1939-43.

12. N. Q. Chinh JL, D. H. Ping, K. Hono. The Effect of Cu on Mechanical and Precipitation Properties of Al-Zn-Mg Alloys. Journal of Alloys and Compounds. 2003;378:52-60.

13. D. A. Porter KEE. Phase Transformations in Metals and Alloys. 2nd ed: Chapman & Hall; 1995.

14. G. Sha AC. Early-stage Precipitation in Al-Zn-Mg-Cu Alloy (7050). Acta Materialia. 2004;52:4503-16.

15. Meng Q. Effect of Cu Content on Corrosion Behavior and Chromate Conversion Coating Protection of 7XXX Series Al Alloys. Ohio: The Ohio State University; 2003.

16. J. D. Robson PBP. Dispersoid Precipitation and Process Modelling in Zirconium Containing Commerial Aluminium Alloys. Acta Mater. 2000;49:599-613.

17. M. Fortier NCP, X.G. Chen, editor. Formation of Primary $ZrAl_3$ Intermetallic Particles in AA7046 Alloy. 11th International Conference on Aluminium Alloys; 2008; Aachen, Germany: Wiley-VCH.

18. Thomas AT, editor. 6th International Conference on Light Metals; 1975; Leoben, Austria, Aluminium-Verlag, Dusseldorf.

19. Meng QJ, Frankel GS. Effect of Cu content on corrosion behavior of 7xxx series aluminum alloys. Journal of the Electrochemical Society. [Article]. 2004;151(5):B271-B83.

20. He. Zhenbo, Yin. Zhimin, Lin. Sen, Deng. Ying, Shang. Baochuan, Zhou. Xiang. Preparation, Microstructure and Properties of Al-Zn-Mg-Sc Alloy Tubes. Journal of Rare Earths. 2010;28(4):641-6.

21. Xu. Guo-fu, Mou. Shen-zhou, Yang. Jun-jun, Jin. Tou-nan, Nie. Zuo-ren, Zhi-min Y. Effect of Rare Earth Element Er on Al-Zn-Mg Alloy. Transactions of Nonferrous Metals Society of China. 2006;16:598-603.

22. Mukhopadhyay AKP, K. S. Kumar, V. Reddy, G. M. Kamat, S. V. Varma, V. K. Key Microstructural Features Responcible for Improved Stress Corrosion Cracking Resistance and Weldability in 7XXX Series Al Alloys Containing Micro / Trace Alloying Additions. Materials Science Forum. 2006;519-521:315-20.

23. R. G. Kelly JRS, D. W. Shoesmith, R. G. Buchheit. Electrochemical Techniques in Corrosion Science and Engineering: Marcel Dekker, Inc.; 2003.

24. Thompson GE, Wood GC. Corrosion: Aqueous Processes and Passive Films: Academic Press London; 1982.

25. Davis JR. Corosion of Aluminium and Aluminium Alloys. Materials Park, OH, USA: ASM Internatioinal; 1991.

26. Pourbaix M. Atlas of Electrochemical Equilibria in Aqueous Solutions. Houston, Texas: National Association of Corrosion Engineers; 1974.

27. Bergmann G, Waugh LT, Paulng L. Acta Cryst. 1957;10:254.

28. Szklarska-Smialowska Z. Pitting Corrosion of Metals1986.

29. Rynders RM, Paik CH, Ke R, Alkire RC. Journal of the Electrochemical Society. 1994;141(6):1439-45.

30. Burstein GT, Shreir LL, Jarman RA. Corrosion: Elsevier Butterworth-Heinemann; 1994.

31. Strehblow H-H. Nucleation and Repassivation of Corrosion Pits for Pitting on Iron and Nickel. Werkst Korros. 1976;27:792.

32. Frankel GS. Pitting Corrosion of Metals a Review of the Critical Factors. Journal of the Electrochemical Society. 1998;145(6):2186-98.

33. Galvele JR. Journal of the Electrochemical Society. 1976;123(4):464-574.

34. Kruger J, Rhyne K. Neuclear and Chemical Waste Management. 1982;3:205.

35. Bohni H, Uhlig HH. Journal of the Electrochemical Society. 1969;116:906.

36. Leckie HP, Uhlig HH. Journal of the Electrochemical Society. 1966;113:1262.

37. Richardson JA, Wood GC. Journal of the Electrochemical Society. 1970;10:313.

38. Heine MA, Pryor MJ. Journal of the Electrochemical Society. 1967;114:1001.

39. Sato N. Electrochimica Acta. 1971;16:1683-92.

40. Hoar TP, Jackob WR. Nature. 1967;216:1299-301.

41. Pessall N, Liu C. Electrochimica Acta. 1971;16:1987.

42. Pride ST, Scully JR, Hudson JL. Journal of the Electrochemical Society. 1994;141:3028.

43. Szklarska-Smialowska Z. Corrosion Science. 1999;41:1743.

44. Hatch JE. Aluminum: Properties and Physical Metallurgy. Metals Park, OH: ASM; 1983.

45. Strehblow H-H, Wenners J. Electrochimica Acta. 1977;22:421.

46. Engell HJ. Electrochimica Acta. 1977;22(987).

47. Beck TR, Alkire RC. Journal of the Electrochemical Society. 1979;126:1662.

48. Alkire RC, Ernsberger D, Beck TR. Journal of the Electrochemical Society. 1978;1382.

49. Tester JW, Isaacs HS. Journal of the Electrochemical Society. 1979;122:1438.

50. Akiyama E, Frankel GS. Journal of the Electrochemical Society. 1999;146:4095.

51. Ramgopal T, Frankel GS. Corrosion. 2001;57:702.

52. Williams DE, Stewart J, Balkwill PH. Critical Factors in Localized Corrosion. The Elctrochemical Society Softbound Proceeding Series. 1992:36.

53. Trueman AR. Corrosion Science. 2005;47(9):2240-56.

54. Cocks FH, Brummer BS. Third quater report by Tyco Labratories, Inc to NASA1967.

55. Dix JEH. Trans ASM. 1950;42:1057.

56. Galvele JR, DeMicheli SM. Corrosion Science. 1970;10:795.

57. Searles JL. Ohio State University; 2000.

58. Buchheit RG, Moran JP, Stoner GE. Corrosion. 1994;50:120.

59. Searles JL, Gouma PI, Buchheit RG. Stress corrosion cracking of sensitized AA5083 (Al-4.5Mg-1.0Mn). Metall Mater Trans A-Phys Metall Mater Sci. 2001;32(11):2859-67.

60. Muller IL, Galvele JR. Corrosion Science. 1977;17:179.

61. Muller IL, Galvele JR. Corrosion Science. 1977;17:995.

62. Moshier WC, Davis GD, Cote GO. Journal of the Electrochemical Society. 1989;136:356.

63. Davis GD, Moshier WC, Fritz TL, Cote GO. Journal of the Electrochemical Society. 1990;137:422.

64. Davis GD, Moshier WC, Long GG, Black DR. Journal of the Electrochemical Society. 1991;138:3194.

65. Davis GD, Shaw BA, Rees BJ, Ferry M. Journal of the Electrochemical Society. 1993;140:951.

66. Szklarska-Smialowska Z. Corrosion Science. 1992;33:1193.

67. Buchheit RG. Journal of the Electrochemical Society. 1995;142:3994.

68. Park JO, Paik CH, Alkire RC, Natishan PM, Kelly RG, Frankel GS, Newman RC. Critical Factors in Localized Corrosion II. Pennington, NJ: The Elctrochemical Society; 1996.

69. Buchheit RG, Boger RK, Carroll MC, Leard RM, Paglia C, Searles JL. JOM. 2001;53:29.

70. Mizuno K, Nylund A, Olefjord I. Corrosion Science. 2001;43:381.

71. Buchheit RG, Grant RP, Hlava PF, Mckenzie B, Zender GL. Journal of the Electrochemical Society. 1997;144:2621.

72. Buchheit RG, Montes LP, Martinez MA, Micheal J, Hlava PF. Journal of the Electrochemical Society. 1999;146:4424.

73. Buchheit RG, Martinez MA, Montes LP. Journal of the Electrochemical Society. 2000;147:119.

74. Buchheit RG, Boger RK, editors. Localized Corrosion Proceedings of the Research Topical Symposium. Corrosion 2001; 2001; Houston, TX: NACE.

75. Dimtrov N, Mann JA, Sieradzki K. Journal of the Electrochemical Society. 1999;146:98.

76. Dimtrov N, Mann JA, Vukirovic M, Sieradzki K. Journal of the Electrochemical Society. 2000;147:3283.

77. Vucmirovic MB, Dimtrov N, Sieradzki K. Journal of the Electrochemical Society. 2002;149:B428.

78. Zhijun Z. Role of Surface Active Layers on Localized Breakdown of Aluminium Alloy 7075: The Ohio State University; 2006.

79. Kotsikos G, Sutcliffe JM, Holroyd NJH. Hydrogen Effects in the Corrosion Fatigue Behaviour of the White Zone of 7xxx Series Aluminium Alloy Welds. Corrosion Science. 2000;42:17-33.

80. Holroyd NJH, Hepples W, Scamans G, editors. Protection of Al-Zn-Mg Welds Against Exfoliation and Stress Corrosion Cracking Using Aluminium Based Metal Spray Coatings. Proceedings to the International Conference and Exposition on Fatigue, Corrosion Cracking, Fracture Mechanics and Failure Analysis; 1985; Salt Lake City, Utah, USA.

81. Gruhl W, editor. International Congress on Aluminium Alloys in the Aircraft Industry 1976; Turin.

82. Doig A. Military Matallurgy 2002.

83. Holroyd NJH, Hepples W, Scamans G, editors. Prevention of Weld Toe Cracking and Exfoliation Corrosion in Al-Zn-Mg Welds. Third International Conference of Environmental Degradation of Engineering Materials; 1987.

84. Kasukawa M, Nakagawa S, Miyamoto K. EUROPEAN PATENT APPLICATION, EP 2 322 310 A1. Nissan Motor Co., Ltd. 2009.